Metamorphic Facies Distribution in the Western Alps Predicted by Petrological-Thermomechanical Models of Syn-Convergent Exhumation

Joshua D Vaughan-hammon, Lorenzo G Candioti, Thibault Duretz, Stefan M Schmalholz

Geochemistry, Geophysics, Geosystems®

AGU ADVANCING EARTH AND SPACE SCIENCE

RESEARCH ARTICLE
10.1029/2021GC009898

Special Section:
Insights into Subduction Zone Processes from Models and Observations of Exhumed Terranes

Metamorphic Facies Distribution in the Western Alps Predicted by Petrological-Thermomechanical Models of Syn-Convergent Exhumation

Joshua D. Vaughan-Hammon[1], Lorenzo G. Candioti[1], Thibault Duretz[2,3], and Stefan M. Schmalholz[1]

[1]Institut des Sciences de la Terre, Bâtiment Géopolis, Quartier UNIL-Mouline, Université de Lausanne, Lausanne, Switzerland, [2]Univ Rennes, CNRS, Géosciences Rennes UMR, Rennes, France, [3]Institut für Geowissenschaften, Goethe-Universität Frankfurt, Frankfurt, Germany

Key Points:

- Local upper-plate extension and serpentinites, a proxy for a weak subduction interface, enable syn-convergent exhumation
- Syn-convergent exhumation generates a continuous metamorphic facies gradient without tectonic mixing (mélange)
- Modeled *P-T* paths, minor erosion, crustal structure, and metamorphic facies distribution agree with Western Alps

Supporting Information:

Supporting Information may be found in the online version of this article.

Correspondence to:

J. D. Vaughan-Hammon,
Joshua.Vaughan-Hammon@unil.ch

Citation:

Vaughan-Hammon, J. D., Candioti, L. G., Duretz, T., & Schmalholz, S. M. (2022). Metamorphic facies distribution in the Western Alps predicted by petrological-thermomechanical models of syn-convergent exhumation. *Geochemistry, Geophysics, Geosystems*, *23*, e2021GC009898. https://doi.org/10.1029/2021GC009898

Received 6 MAY 2021
Accepted 20 JUN 2022

Abstract The distribution of metamorphic rocks throughout the western European Alps indicates subduction-related metamorphism. However, processes by which high-grade metamorphic rocks exhume remain disputed. Here, we present two-dimensional petrological-thermomechanical numerical models to investigate the metamorphic facies evolution during orogenesis. We model closure of an oceanic basin with exhumed mantle bounded by passive margins. To ensure thermomechanical feasibility, we model also this basin configuration. Before convergence, we replace the uppermost portions of exhumed mantle with serpentinite. Location and orientation of subduction are not predefined and subduction initiates self-consistently during convergence. A weak subduction interface develops if serpentinite is initially thick enough (here 6 km) and can distribute along the interface. Syn-convergent exhumation of (ultra)high-pressure rocks occurs with minor erosion, enabled by local upper-plate extension and a crustal-scale normal-sense shear zone. We calculate metamorphic facies evolutions with peak P and T values of 10,000 markers. Results show (a) peak P and T values agreeing with estimates from natural rocks, (b) exhumed, structurally coherent regions with identical metamorphic facies, indicating absence of significant mixing (mélange), (c) facies distributions corresponding to that of the Western Alps, which is from eclogite to blueschist to greenschist facies when going from internal to external domains, and (d) exhumation velocities larger than burial velocities. Models with stronger subduction interface (3-km serpentinite thickness) develop an orogenic wedge with vertical metamorphic gradient and minor exhumation. Syn-convergent exhumation is feasible for the Western Alps and calculating metamorphic facies distribution is useful when testing the applicability of models to natural orogens.

Plain Language Summary Evidence for deep geological processes (>c. 50 km) can be found in places throughout the Earth's surface where tectonic plates have converged and crustal rocks have been buried and subsequently exhumed back to the surface. Collision zones, such as those found in the western European Alps, provide a record of plate convergence and the associated burial-exhumation history. The pattern of mineral changes due to pressure and temperature conditions (so-called metamorphic facies) provides clues for the burial and exhumation history of rocks and, hence, for the geodynamic evolution of mountain belts. In the Western Alps, rocks with the highest metamorphic grade, indicating the most extreme burial and exhumation history, are closest to the observed collision front. This study presents results of two-dimensional computer simulations, which are based on fundamental laws of physics, laboratory experiments, and natural observations. These simulations predict the evolution of the large-scale metamorphic facies architecture of the Western Alps during continuous plate convergence.

1. Introduction

The dynamic nature of the Earth's crust has become clearer since the observation of regional-scale systematic changes in index minerals (Barrow, 1893), the subsequent conceptualization of metamorphic facies (Eskola, 1915), and the recognition of plate tectonics (e.g., Isacks et al., 1968; Le Pichon, 1968; Morgan, 1968; Wegener, 1915). Observations show that regions of crustal convergence have unique metamorphic facies sequences linked to specific tectonic processes (Miyashiro, 2012). High-grade rocks exhumed in mountain belts provide an ideal place to reconstruct deep tectono-metamorphic processes and subduction interface dynamics. In the European Alps, the distribution of metamorphic facies allows us to identify (a) the spatial distribution of exhumed rocks

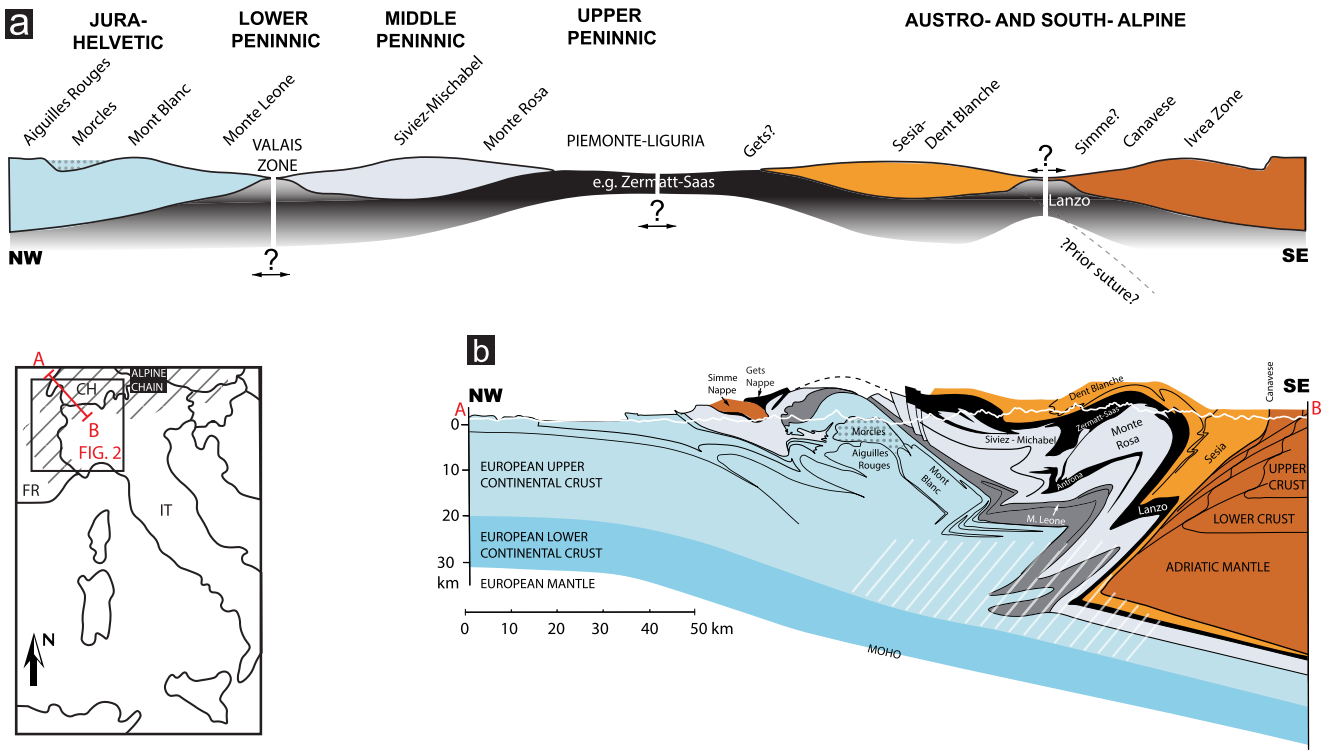

Figure 1. (a) Simplified paleogeographic cross-section reconstruction of the western Alpine Tethys domain between the Adriatic and European margin prior to convergence (distorted horizontal and vertical scales), modified after Dal Piaz et al. (2001) and McCarthy et al. (2020). (b) Simplified present-day cross section of the Western Alps colored with respect to the paleogeographic domains in panel (a), modified after Escher et al. (1993) and Steck et al. (2015) (structure of white shaded area is not well constrained). The location of the cross section is indicated on the map in the lower left part of the figure.

that have been metamorphosed under similar pressure and temperature conditions (e.g., Bousquet et al., 2008; Frey et al., 1999; Lardeaux, 2014), (b) the ancient subduction direction (e.g., Ernst, 1971), and (c) the spatial evolution of metamorphism through time (e.g., Lardeaux, 2014).

The vast number of field and geophysical studies as well as advancements in dating metamorphism, in thermodynamic methods and in deterministic modeling, has significantly improved our understanding of the tectono-metamorphic evolution of the Western Alps (Figures 1 and 2). Nevertheless, major questions remain open regarding, for example, the exhumation mechanisms. For example, some studies suggest that rock exhumation in the Western Alps can occur during continuous plate convergence, so-called syn-convergent exhumation (e.g., Agard, 2021; Butler et al., 2014; Escher & Beaumont, 1997). In contrast, other studies argue that syn-convergent exhumation is not feasible because it requires unrealistically large erosion for the Western Alps (e.g., Malusà et al., 2015). Such studies suggest that exhumation occurs during periods of plate divergence (e.g., Liao et al., 2018; Malusà et al., 2015). Here, we investigate the metamorphic facies evolution and distribution for syn-convergent exhumation to test whether syn-convergent exhumation can occur without significant erosion and can generate a metamorphic facies distribution, which is comparable to that of the Western Alps. Other disputed issues concerning the Alpine orogeny include, for example, (a) the heat budget during Barrovian metamorphism in the Lepontine dome (Berger et al., 2011; Burg & Gerya, 2005; Jamieson et al., 1998; Ryan & Dewey, 2019; Stüwe, 1998), (b) potential local deviations from lithostatic pressure (Luisier et al., 2019; Schenker et al., 2015; Vaughan-Hammon et al., 2021b), and (c) the mechanisms by which small volumes of ultrahigh-pressure (UHP) rocks are exhumed and embedded in lower grade high-pressure (HP) units, for example, the *c*. 1 km thick Brosasco-Isasca UHP Unit within the HP Dora Maira massif (e.g., Bonnet et al., 2022; Chopin, 1987; Groppo et al., 2019; Hacker & Gerya, 2013; Kurz & Froitzheim, 2002; Schmalholz & Schenker, 2016; Warren, 2013). With the aim of contributing to eventually resolving the issues mentioned above, we also (a) investigate the temporal relation between peak pressure and peak temperature for pressure-temperature-time (*P*-*T*-*t*) paths, and (b) study the relation between the metamorphic grade of exhumed rocks and their original paleogeographic position.

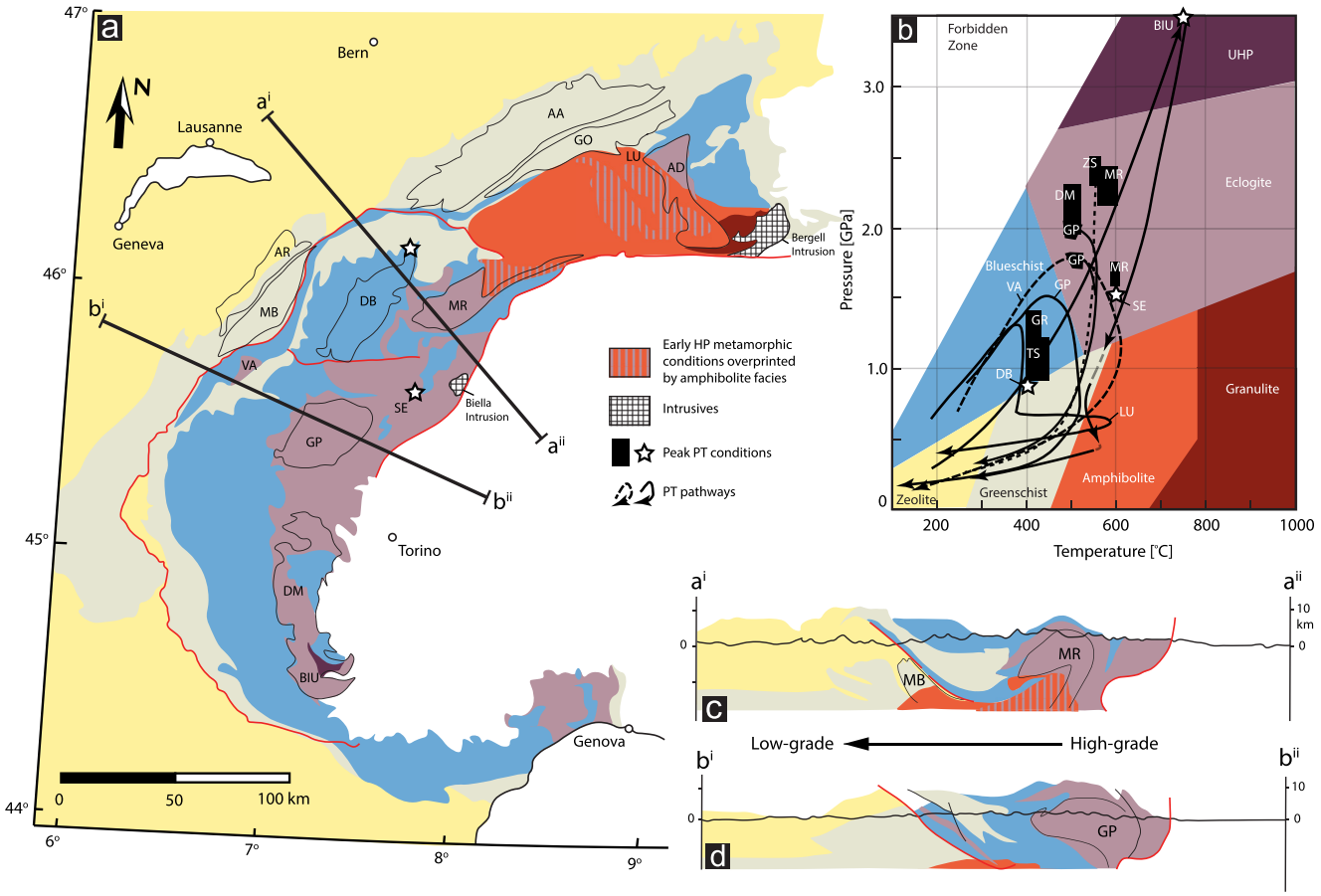

Figure 2. (a) Simplified map of peak Alpine metamorphic facies distribution throughout the Western Alps with major units indicated, modified after Oberhänsli et al. (2004) and Bousquet et al. (2008) (AA = Aar massif, GO = Gotthard massif, LU = Lucomagno, AD = Adula, MR = Monte Rosa, DB = Dent Blanche, GP = Gran Paradiso, DM = Dora Maira, BIU = Brossasco-Isasca unit, SE = Sesia, VA = Valaisan, MB = Mont Blanc massif, AR = Aiguilles Rouge massif). (b) Approximate pressure-temperature metamorphic facies grid (modified after Philpotts & Ague, 2009) with representative *P-T* estimates for Western Alpine units (dashed and solid lines are used for clearer visualization), BIU = (Rubatto & Hermann, 2001), MR = (Luisier et al., 2019; Vaughan-Hammon et al., 2021b), SE = (Lardeaux et al., 1982; Vuichard & Ballevre, 1988), VA = (Bousquet et al., 2002; Goffé & Bousquet, 1997; Wiederkehr et al., 2007), GP = (Bousquet et al., 2008; Manzotti et al., 2018), LU = (Wiederkehr et al., 2008), DB = (Cortiana et al., 1998), DM = (Groppo et al., 2019), TS = Tambo Suretta (Challandes et al., 2003), ZS = Zermatt-Saas (Angiboust et al., 2009), GR = Grisons (Bousquet et al., 2002). (c and d) Simplified cross sections of peak metamorphic facies with direction of decreasing subduction-related metamorphism indicated.

Many petrological studies have compiled large data sets of subduction-related peak metamorphism for the entire Alps (e.g., Bousquet et al., 2008). Based on this data, many burial and exhumation cycles for rocks in the Alps, as well as their distribution through time and space, have been suggested in the past (e.g., Bousquet et al., 2008; Lardeaux, 2014). Both petrological and age data provide ample resources to test the validity of such burial and exhumation cycles. Furthermore, deterministic numerical models can be used to test the physical feasibility of proposed burial and exhumation cycles. Deterministic numerical models are based on fundamental laws of physics, which are expressed by a system of partial differential equations describing conservation of mass, momentum, and energy, and incorporate mechanical properties and flow laws derived from laboratory rock deformation experiments. Such numerical models have been applied to investigate the mechanisms of exhumation of (U)HP rocks within Alpine-type collisional belts (e.g., Burov et al., 2001; Butler et al., 2014; Gerya et al., 2002; Ruh et al., 2015; Stöckhert & Gerya, 2005; Warren et al., 2008; Yamato et al., 2008, 2007). Several of these studies trace individual numerical markers (e.g., Gerya & Yuen, 2003) in order to assess *P-T-t* trajectories during syn-convergent exhumation (e.g., Butler et al., 2014; Gerya et al., 2002; Regorda et al., 2021; Ruh et al., 2015; Stöckhert & Gerya, 2005; Warren et al., 2008; Yamato et al., 2008, 2007). Although such numerical models successfully reproduce individual exhumation *P-T-t* trajectories that are comparable to the Alps (e.g., Butler et al., 2014; Gerya & Yuen, 2003; Ruh et al., 2015; Warren et al., 2008; Yamato et al., 2008, 2007),

only few numerical modeling studies (e.g., Butler et al., 2014; Regorda et al., 2021) attempted to reproduce the spatially continuous distributions of metamorphic facies and the entire, regional-scale metamorphic architecture of the Western Alps (Figure 2). If only individual markers are traced, it is not possible to determine (a) whether exhumed rock units underwent significant tectonic mixing and (b) whether the exhumed rocks form a regional trend of metamorphic facies, which is comparable to that of the Western Alps. Therefore, we use here a petrological-thermomechanical numerical model to trace pressure and temperature of *c*. 10,000 numerical markers for each simulation. We use the *P-T* record from these markers to generate cross sections showing the metamorphic facies distribution after syn-convergent exhumation, which we compare to published metamorphic facies distributions.

Furthermore, common to most published models is that the initial geometry of the ocean basin and passive margins is predefined ad hoc and/or that the location and orientation of the subduction zone is predefined by a prominent weak zone across the modeled lithosphere (e.g., Butler et al., 2014; Warren et al., 2008; Yamato et al., 2008). Here, we do not predefine ad hoc the passive margin geometry and do not employ a weak zone to predefine subduction initiation. In contrast, we model the preconvergence basin and passive margin geometry with a numerical simulation (e.g., Candioti et al., 2021; Petri et al., 2019). During subsequent convergence of the basin-passive margin system, subduction initiates self-consistently by strain localization due to local thermal softening, which was shown recently by several numerical studies (e.g., Auzemery et al., 2020; Candioti et al., 2021, 2022; Kiss et al., 2020). The motivation for not prescribing ad hoc the preconvergence basin geometry and a prominent weak zone is that we want to predetermine as little as possible the modeled subduction zone and the associated burial and exhumation cycles. In other words, we want to test the feasibility of syn-convergent exhumation with numerical models in which none of the main features controlling the burial-exhumation cycle are predefined (e.g., a weak zone controlling the location and orientation of subduction zone initiation or a weak interface of an already existing subduction zone).

Moreover, many studies highlight the importance of mechanically weak serpentinite for the exhumation of (U)HP rocks (e.g., Agard et al., 2018; Candioti et al., 2020, 2021; Guillot & Hattori, 2013; Guillot et al., 2015; Ruh et al., 2015; Schwartz et al., 2001). Serpentinite presumably contributes to the weakening of the plate interface during subduction (e.g., Agard et al., 2018; Hess, 1955; McCarthy et al., 2020), assisting the exhumation of buoyant crustal units (Agard et al., 2018; Guillot & Hattori, 2013; Guillot et al., 2015; Ruh et al., 2015). However, the detailed rheological properties of serpentinite during subduction are still not well constrained (e.g., Amiguet et al., 2014; Guillot & Hattori, 2013; Guillot et al., 2015; Hilairet et al., 2007; Hirth & Kohlstedt, 2003). Here, we also investigate the impact of serpentinite on exhumation and the resulting spatio-temporal distribution of metamorphic facies. We account for ocean floor serpentinization by including a low-strength layer at the top of the exhumed mantle lithosphere, prior to imposing plate convergence. We do not model in detail the serpentinization process (e.g., latent heat, hydration reaction, fluid flow, etc.).

2. Tectono-Metamorphic Evolution of the Western Alps

The present-day large-scale tectonic architecture of the Western Alps is derived from the convergence and ultimate collision of the formerly hyper-extended margins of the northern Adriatic continent and southern European continent (Figure 1). Subduction presumably started in the distal parts of the Adriatic margin and persisted from the late-Cretaceous (85–65 Ma, Sesia-Lanzo zone: Duchêne et al., 1997; Engi et al., 2011; Inger et al., 1996; Manzotti, Ballevre, et al., 2014; Rubatto et al., 1999) to the late-Eocene (35–32 Ma, Dora Maira: Di Vincenzo et al., 2006; Duchêne et al., 1997; Gebauer et al., 1997; Tilton et al., 1989). Later-stage folding events (e.g., *c*. 40–35 Ma, Mischabel folding: Barnicoat et al., 1995; Keller et al., 2005; Steck et al., 2015) combined with earlier subduction-related nappe emplacement resulted in the current tectonic configuration (Figure 1b). Geological cross sections can be constructed due to the strong Alpine topography, axial plunges of exhumed units, and interpretation of high-resolution seismic data (e.g., Escher & Beaumont, 1997; Escher et al., 1993; Malusà et al., 2021; S. Schmid & Kissling, 2000; S. M. Schmid et al., 2017; Steck et al., 2015). Paleogeographic reconstructions of the Western Alps (e.g., Dal Piaz et al., 2001; De Graciansky et al., 2011; Lemoine et al., 1986; McCarthy et al., 2020; S. M. Schmid et al., 2004; Steck et al., 2015; Trümpy, 1975) define five main domains (Figure 1a): (a) the structurally highest Adriatic margin consisting of the Ivrea Zone and Sesia-Dent Blanche continental units, presumably separated by the exhumed sublithospheric mantle (e.g., Lanzo peridotites) from the main Adriatic margin, (b) the Piemonte-Liguria Oceanic domain, or upper Penninic, separating Adria and Europe

(e.g., Zermatt-Saas ophiolites), (c) the Briançonnais, or middle Penninic (e.g., Monte Rosa and Siviez-Mischabel units), (d) the Valais Zone, or lower Penninic, with units of sublithospheric mantle (e.g., Geisspfad peridotites), and (e) the Jura-Helvetic domain including the external crystalline basement massifs (e.g., Mont Blanc) and sedimentary cover series (e.g., Morcles nappe).

Widespread occurrences of deeply subducted oceanic domains, such as the former Piemonte-Liguria Ocean (e.g., Zermatt-Saas ophiolites) comprises significant proportions of serpentinite (*c*. 50%, e.g., Angiboust et al. (2009)). Continental internal crystalline massifs, such as the Monte Rosa units, are almost entirely enveloped in serpentinite-bearing oceanic domains (Zermatt-Saas and Antrona units; Figure 1b). The presence of serpentinite-bearing oceanic domains is presumably important for the Alpine orogeny, due to its relatively lower density and viscosity compared to surrounding crustal and mantle rocks (e.g., Angiboust et al., 2009; Forster et al., 2004; Hess, 1955; McCarthy et al., 2020).

Metamorphic zoning follows the arcuate shape of the Western and Central Alpine mountain belt (Figure 2a). Throughout the Western Alps, metamorphic facies conditions related to subduction are observed, from UHP to greenschist facies (Figures 2a and 2b; Berger & Bousquet, 2008; Bousquet et al., 2008; Oberhänsli et al., 2004). Studies from the early 1970s provide the first overview of the metamorphic facies distribution in the Alps (Ernst, 1971) and a first overview of the mineralogy and distribution of metamorphic indicators was provided in the 26th International Geological Congress (Saliot et al., 1980), although UHP rocks were not identified until a few years after (e.g., Agard, 2021; Chopin, 1984). Soon after, it was becoming more apparent that there exists a regional metamorphic trend, with an internal zone of HP domains and decreasing metamorphic grade toward the external, foreland basin direction (Figures 2a, 2c and 2d; see also recent review by Agard (2021)).

Figure 2 shows a simplified distribution of metamorphic rocks within the Western Alps, modified after Oberhänsli et al. (2004) and Bousquet et al. (2008), based on approximate pressure and temperature ranges for basic metamorphic facies (Philpotts & Ague, 2009). Petrologically determined pressure-temperature pathways for a range of lithologies and from various locations within the Western Alpine metamorphic belt typically exhibit clockwise burial and exhumation pathways (Figure 2b). This subduction-related metamorphism is, in some places, overprinted by a thermally dominated metamorphic event, for example, Lucomagno nappe heating during decompression (LU in Figure 2b; Wiederkehr et al., 2008). This thermal perturbation within the Central Alps is known as the Lepontine Dome, and is characterized by a metamorphic domal structure of concentric thermal isograds (e.g., Steck & Hunziker, 1994) that presumably crosscut early Alpine HP, low-temperature nappe boundaries of the Penninic units (e.g., Burg & Gerya, 2005). This heating event reaches amphibolite to granulite facies conditions *c*. 600°C ± 150°C (e.g., Engi et al., 1995) dated between 40 and 30 Ma (e.g., Schlunegger & Willett, 1999), as well as local anatexis in the southern Central Alps close to the late Alpine Bergell intrusion (32.8–22 Ma: Gianola et al., 2014; Gregory et al., 2009; Oberli et al., 2004; Rubatto et al., 2009; von Blackenburg, 1992). In cross section, late-Alpine thermal overprinting is mainly confined to rocks derived from the subducting European plate (Figure 2c; Bousquet et al., 2008). Compared to earlier subduction-related metamorphism, the mechanisms for the late thermal event are still disputed, with interpretations including viscous heating or increased radiogenic heat production (e.g., Burg & Gerya, 2005; Jamieson et al., 1998).

3. Numerical Model

3.1. Model Approach and Overview

We apply a numerical model to simulate the convergence of a marine basin with exhumed mantle that is bounded by two magma-poor passive margins (Figure 3b). We do not design this initial basin configuration ad hoc, but generate this basin configuration with a lithospheric rifting simulation using the same numerical model. The model characteristics such as the size of the basin, the rifting and convergence velocities, or the duration of rifting and convergence are chosen to be applicable to the Western Alpine orogeny, which likely resulted from a Wilson Cycle involving an embryonic ocean (e.g., Candioti et al., 2021; Beaussier et al., 2019; Chenin et al., 2019; Erdős et al., 2019; J. F. Dewey & Burke, 1974; Mohn et al., 2010; Wilson, 1966). The term embryonic implies that the ocean basin mainly formed by ultraslow spreading without the generation of significant mature oceanic crust (e.g., McCarthy et al., 2020). Although the numerical simulation covers an entire extension-convergence cycle, we focus here only on the last stages of the convergence period involving subduction and exhumation of continental crust. Our modeling approach is, hence, different from most previous numerical models as we do not

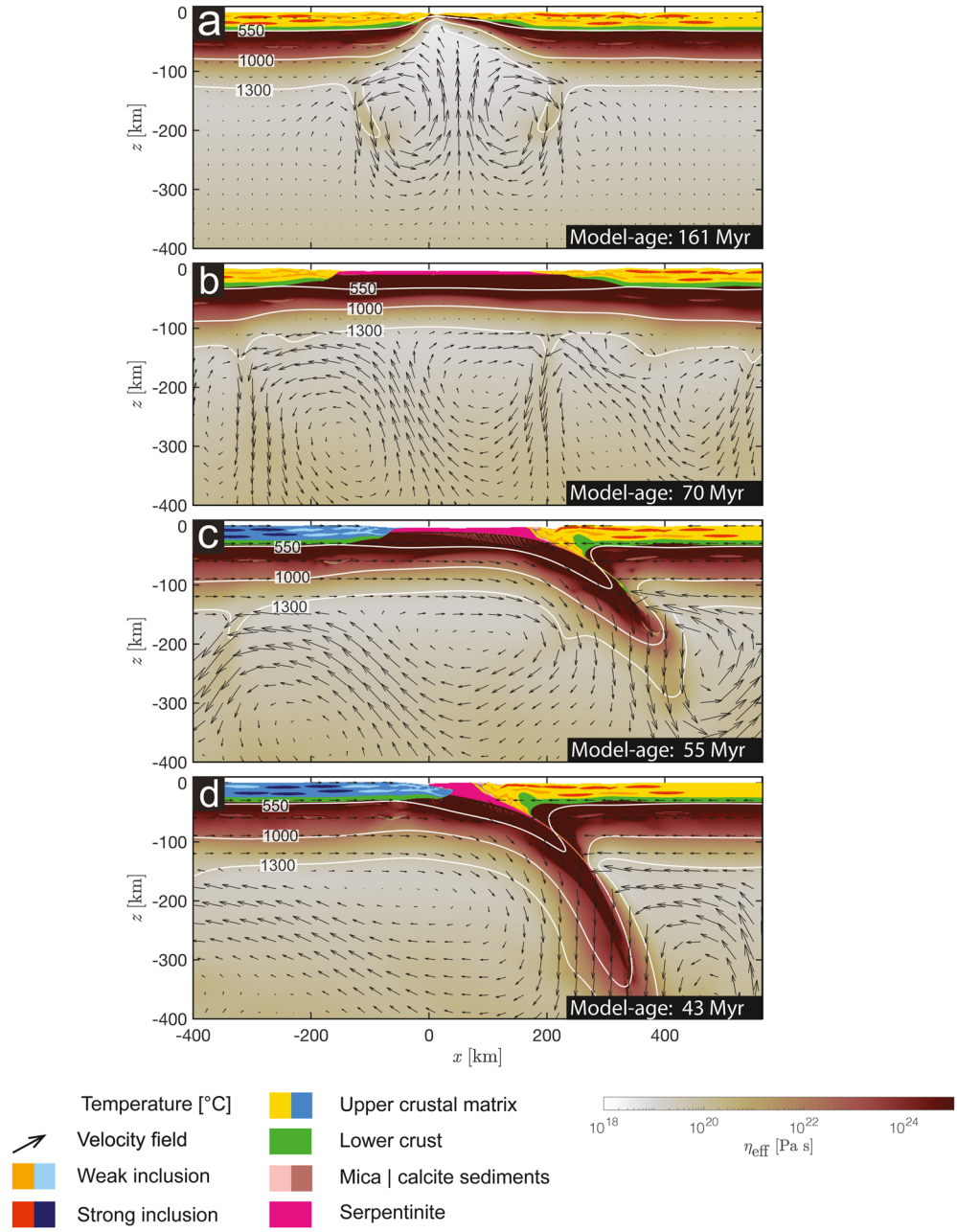

Figure 3. Numerical results showing the evolution of model units and effective viscosity (η_{eff}) of the mantle prior to continental collision. (a) Rifting of continental lithosphere and exhumation of the mantle. (b) End of thermal relaxation phase and serpentinization of upper portions of exhumed mantle. (c) Convergence of model and single-sided subduction initiated below distal portions of a hyper-extended continental margin. Colors of continental units changed to blue for subducting plate in order to delimit and imitate the European margin subducting below Adria (Figure 1). (d) Closure of ocean basin and onset of subduction of continental crust.

prescribe ad hoc the preconvergence passive margin architecture and a prominent trans-lithospheric weak zone to predetermine the location and orientation of the subduction zone.

We first simulate the initial basin configuration with two subsequent model periods: (a) Extension for 50 Myr of a continental lithosphere with initially constant thickness (see Table S1 and Figure S1 in Supporting Information S1), which leads to the formation of asymmetric passive continental margins bounding a marine basin floored by exhumed mantle (Duretz et al., 2016; Petri et al., 2019; Figure 3a). We apply 1.0 cm yr^{-1} absolute boundary

velocity during extension, which corresponds approximately to the average extension velocities during Alpine Mesozoic rifting (Le Breton et al., 2021). (b) A 60 Myr long period without far-field extension or convergence allowing for thermal equilibration of the evolved basin-margin system (e.g., Le Breton et al., 2021; Figure 3b). At the end of this cooling period, we parameterize a serpentinization front at the upper portions of the mantle exhumed in the basin (e.g., McCarthy et al., 2020). The simulated basin configuration, involving the serpentinite, serves as initial model configuration for the convergence simulation.

Figure 3b displays the initial configuration for the convergence simulation, which is separated into two periods: (a) Convergence is applied with 1.5 cm yr^{-1} absolute boundary velocity for 30 Myr to model plate boundary formation by subduction initiation and basin closure (e.g., Handy et al., 2015; J. Dewey et al., 1989; Manzotti, Ballevre, et al., 2014; S. M. Schmid et al., 1996; Figure 3c). (b) The applied boundary velocity is reduced to 1.0 cm yr^{-1} for the rest of the simulation when the continental crust of the lower plate starts subducting. Subduction and exhumation of continental crustal rocks takes place during this period with reduced convergence velocity (e.g., Handy et al., 2015; S. M. Schmid et al., 1996; Figure 3d), which is the main focus of our study.

3.2. Numerical Algorithm and Model Configuration

The applied petrological-thermomechanical model is a state-of-the-art model for lithosphere and upper mantle deformation (Candioti et al., 2020, 2021; Duretz et al., 2016; Petri et al., 2019). The model considers visco-elasto-plastic incompressible deformation, gravity, heat transfer, a simple erosion model, and thermodynamically constrained densities. The mathematical model, the numerical algorithm, and its calibration to the lithosphere-upper mantle system are described in detail in the open-access articles of Candioti et al. (2020, 2021). We therefore do not describe these details here again but, for completeness, provide a detailed description of the applied petrological-thermomechanical model in Supporting Information S1.

The initial model configuration for the extension model consists of a model domain with dimensions 1,600 × 680 km (Figure S1 in Supporting Information S1). We employ a global numerical resolution of 1 × 1 km. Modeled units include a 25 km thick mechanically heterogeneous upper crust and a 8 km thick homogeneous lower crust (Figures S1b and S1c in Supporting Information S1). Heterogeneities in the upper crust are modeled with initially elliptical regions having different mechanical properties than the surrounding, background crust (see Figure S1c in Supporting Information S1; see also Candioti et al. (2021)). The lithospheric mantle extends down to 120 km depth and we include the upper mantle down to a depth of 660 km. The upper regions of the mantle lithosphere also contain heterogeneities with different mechanical properties compared to the surrounding mantle (see Figure S1c in Supporting Information S1; see also Candioti et al. (2021)).

After the extension and cooling period (Figures 3a and 3b), the upper crust is separated by a basin with exhumed mantle lithosphere. The top of the exhumed mantle is replaced by a layer of serpentinite with different thickness, either 3, 5, or 6 km. Based on this initial configuration, we performed a systematic analysis of 18 numerical simulations, which test the impact of three parameters on the subduction and exhumation dynamics: (a) continental crustal strength using a flow law of either Westerly granite or wet anorthite, (b) degree of parameterized serpentinization by applying different initial serpentinite thickness (3, 5, or 6 km), and (c) different convergence velocities after basin closure (see Figures S3 and S4 in Supporting Information S1). The applied flow laws for the lower crust (wet anorthite), mantle lithosphere (olivine), the initially elliptical heterogeneities, and serpentinite (antigorite) are specified in Table S1 in Supporting Information S1. From these 18 simulations, we selected two representative simulations: the flow law for the crust is that of Westerly granite, the convergence velocity after basin closure is 1.0 cm yr^{-1} but the initial serpentinite thickness is either 3 or 6 km. We chose these two simulations because they show two endmember scenarios for orogenic wedge formation applicable to the Western Alps: (a) an orogenic wedge without significant exhumation (for 3-km serpentinite thickness) and (b) an orogenic wedge with significant exhumation (for 6-km serpentinite thickness; Figure 4, the results are discussed in detail in Section 4). For the simulation with 6-km serpentinite thickness (Table S1 in Supporting Information S1), we also performed four additional simulations with different properties of the crustal heterogeneities in the subducting crust to investigate the impact of these heterogeneities on the burial and exhumation dynamics (Figure 5 and Figure S6 in Supporting Information S1).

For the convergence simulations, the variation of the density with pressure and temperature is calculated before the simulations for all model units with Perple_X phase equilibria models (Connolly & Petrini, 2002). The

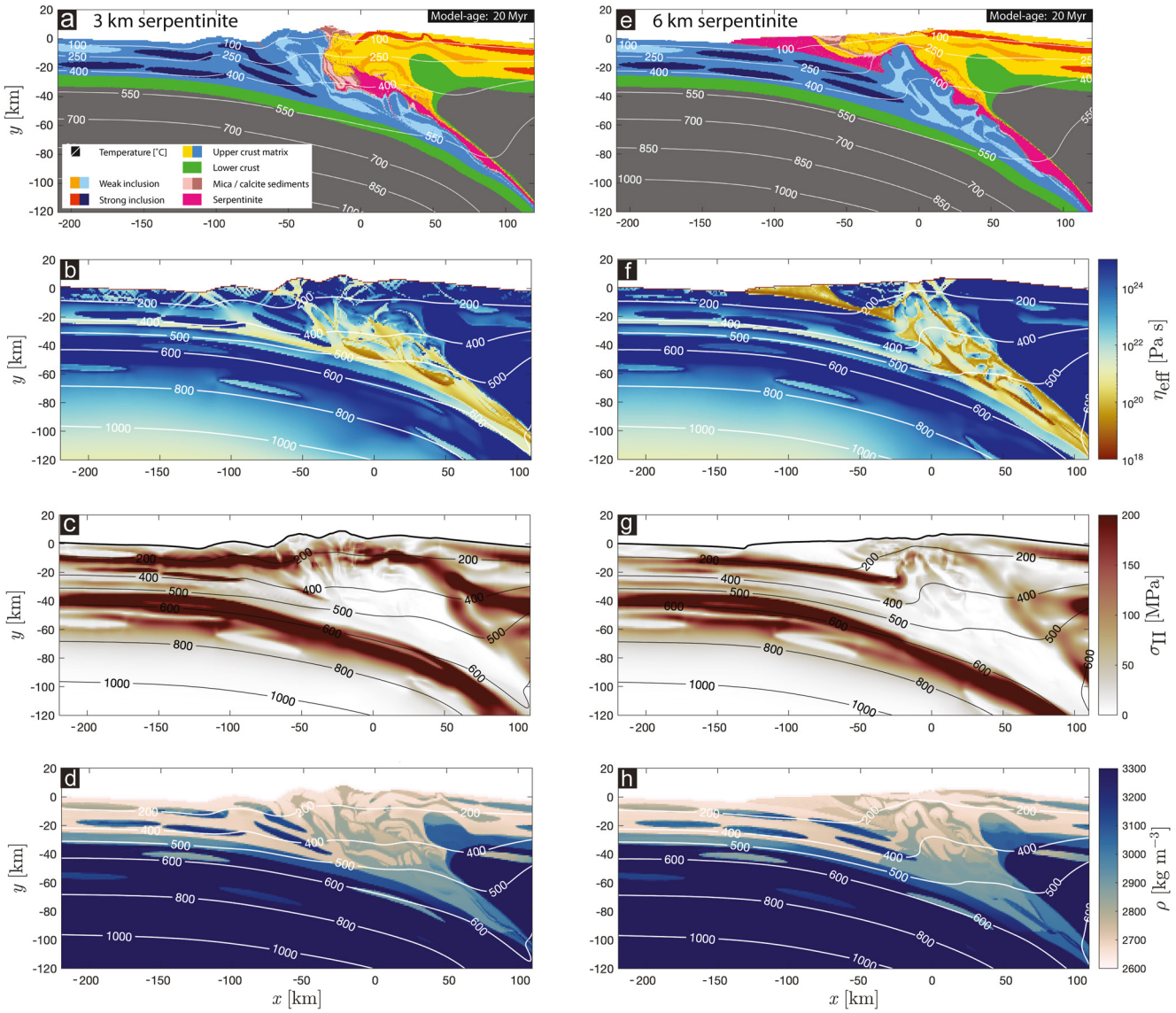

Figure 4. Numerical results showing several characteristics of the subduction interface during continental collision for simulations with initially 3-km serpentinite thickness (left column) and 6-km thickness (right column). (a and e) Model units. (b and f) Effective viscosity (η_{eff}), highlighting the low-viscosity plate interface propagating to the surface in the 6-km serpentinite model. (c and g) Square root of the second invariant of the deviatoric stress tensor (σ_{II}). (d and h) Density distribution (ρ). Scientific color maps used are provided by Crameri (2018).

average bulk rock compositions assumed for the model units are given in Table S2 in Supporting Information S1 and the employed phase diagram density fields are displayed in Figure S2 in Supporting Information S1.

The term "model-age (Myr)" presented in each figure denotes the use of simulated time being analogous to geological time used in many petrological studies, whereby the present day is regarded as 0 million years ago (Ma) and increases positively into the past. In this study, we adopt the same approach, whereby the final time step has a model-age of 0 Myr. When applying the presented models to the Western Alps, the relative timescale of events should be considered. The absolute "model-ages" are of no significance, and 0 Myr (for the end of each simulation) has been chosen to aid comparison of timescales of orogenic activity, and therefore, should not be compared with absolute timing in the geological history of the Alps.

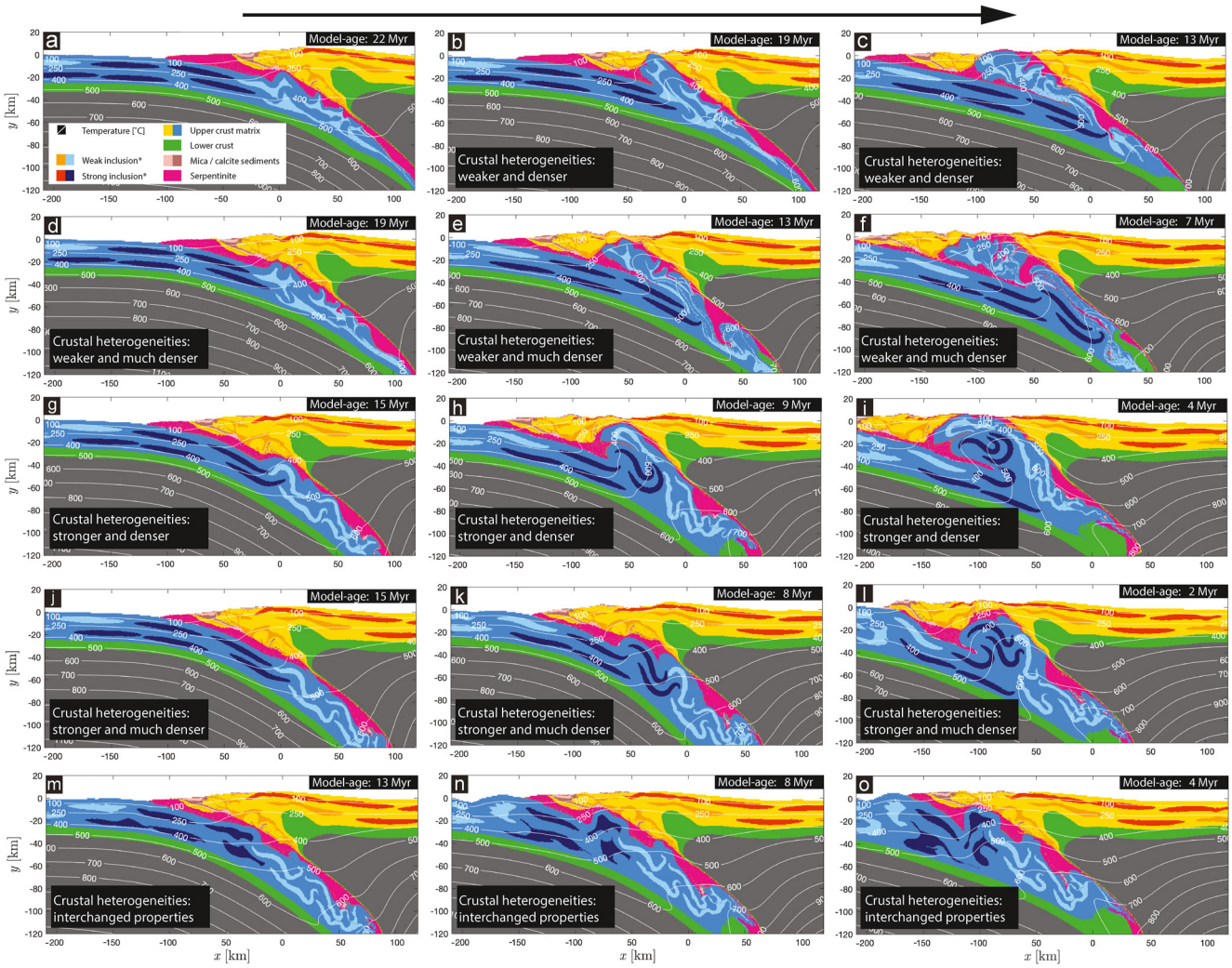

Figure 5. Numerical results showing the evolution of model units and isotherms for models with 6-km serpentinite thickness and varying properties of crustal heterogeneities in the distal regions of the subducting plate (light blue units). (a–c) Weaker and denser heterogeneities in the distal portions of the subducting plate, compared to the background upper crust (referred to as standard configuration in the text; physical properties are given in Supporting Information S1). (d–f) Weaker and much denser crustal heterogeneities. (g–i) Stronger and denser crustal heterogeneities. (j–l) Stronger and much denser crustal heterogeneities. (m–o) The properties of the light blue heterogeneities (standard configuration) have been interchanged with the properties of the more proximal, dark blue heterogeneities (stronger and much denser; standard configuration). Color plots of densities and effective viscosities are displayed in Figures 4f, 4h and Figure S6 in Supporting Information S1.

3.3. Defining Numerical Metamorphic Facies

To assess the distribution of metamorphic facies within the modeled orogen, *P-T-t* histories for numerical markers are analyzed. A Marker-in-Cell method (Gerya & Yuen, 2003) is employed to transport physical properties throughout the numerical grid. Nearly 56 million Lagrangian markers are used to transport physical properties at each time step. From the 56 million markers in total, *c*. 10,000 representative markers are chosen for each simulation from the continental passive margin of the subducting plate prior to subduction. Following the *P-T* trajectory of markers during subduction, the maximum values of *P* and *T* are used to define a metamorphic facies (Figure 2b). This metamorphic facies identity at peak conditions is then stored for each individual marker regardless of its position during subsequent exhumation. Although a simplified metamorphic facies grid (Philpotts & Ague, 2009), that is neglecting subdivision such as upper greenschist facies and blueschist subdivisions etc., the main subdivisions are captured, for example, eclogite-UHP transition defined by quartz-coesite. Also, a limiting geothermal gradient of 5°C/km for the forbidden zone conditions is illustrated for clarity in Figure 2b. These metamorphic facies divisions are similar to those used in studies characterizing the metamorphic structure of metasediments throughout the European Alps (Figure 2; e.g., Bousquet et al., 2008).

Since we are assessing subduction-related metamorphism, that is peak-metamorphic conditions, several assumptions are made. First, a major assumption is that peak-metamorphic conditions define an equilibrium state in a rock, and thus peak-metamorphic rates are attained at peak conditions (e.g., Spear, 1989). Second, rocks defined by facies domains are assumed to be saturated and in equilibrium with water. Third, we do not define transition zones between facies that could correspond to variations in bulk rock compositions or kinetic factors, which is a mixture of the above-mentioned assumptions (Philpotts & Ague, 2009). Overall, we do not numerically model mineral assemblages that evolve during changing *P-T* conditions, rather, we infer the range of *P-T* conditions that would define an assemblage. This enables us to build a picture of the relative *P-T* conditions for subducted and exhumed continental rocks (Ghent, 2020).

A caveat of this approach is that the maximum *P* and maximum *T* of *P-T* pathways rarely correspond to the same point in *P-T* space. Therefore, we evaluate two peak metamorphic condition scenarios: (a) maximum *T* and corresponding *P* (herein referred to as max. *T*), and (b) maximum *P* and corresponding *T* (herein referred to as max. *P*). For each numerical simulation, we present the results for both facies based on the max. *P* or max. *T*. A graphical representation of the difference between the max. *P* and max. *T* facies and the resulting metamorphic facies identity can be found in Figure S5 in Supporting Information S1.

4. Results

4.1. Preconvergence Situation and Subduction Initiation

Lithospheric extension leads to crustal breakup and the formation of two conjugate asymmetric magma-poor continental margins (Figures 3a and 3b). After cooling at 70 Myr, a *c*. 360 km wide marine basin has formed, which is floored by exhumed mantle (Figure 3b). Thermal convection in the upper mantle has stabilized the thermal and mechanical thickness of the lithosphere to *c*. 120–140 km (region without velocity glyphs in Figure 3b). At the end of the cooling period, the top 3 or 6 km of the exhumed mantle are replaced by material properties of serpentinite (Table S1 in Supporting Information S1). The extension and cooling period has generated a configuration of a basin with exhumed mantle bounded by two asymmetric passive margins with the following characteristics: (a) the basin-passive margin geometry is thermomechanically feasible, (b) the basin-passive margin system is mechanically and isostatically stable since there are no significant horizontal and vertical displacements during the cooling period, (c) an equilibrium conductive geotherm has established across the lithosphere and stable thermal convection cells have stabilized an average adiabatic thermal gradient in the upper mantle (see also results of Candioti et al. (2020)), and (d) there are no major predefined weak zones across the lithosphere. This simulated basin-passive margin configuration serves as initial configuration for the convergence simulations.

During the early stages of convergence, subduction initiation is horizontally forced and caused by strain localization due to thermal softening (for more information see Auzemery et al. (2020), Candioti et al. (2021, 2022), and Kiss et al. (2019, 2020)). Subduction initiation occurs below the distal portions of one continental hyper-extended margin (Figure 3c). The location and polarity of subduction initiation is not prescribed, but develops spontaneously in both models with a 3- and 6-km serpentinite layer thickness. Subduction initiation is, hence, a self-consistent thermomechanical feature of the converging basin-passive margin system. Furthermore, the characteristics of the emerging subduction plate interface have not been predefined and this interface also emerges in a spontaneous manner. During basin closure and subduction, the serpentinites are strongly deformed, partly sheared off the subducting slab, and eventually reorganize along the subduction interface (Figure 3d). In this study, we focus on the model evolution after basin closure, starting from the onset of subsequent subduction of continental crust during the final 40 Myr (Figures 4 and 5).

4.2. Subduction and Syn-Convergent Exhumation

Figure 4 highlights the main characteristics of the subduction plate interface during subduction and orogenic wedge formation. For both models with initially 3- and 6-km thick serpentinite, a weak plate interface, having an effective viscosity of less than *c*. 10^{20} Pas, develops in depths larger than *c*. 25 km (Figures 4b and 4f). The situation is different for the uppermost 25 km. For the 3-km serpentinite model, a weak plate interface with low effective viscosity ($<10^{20}$ Pas) is unable to develop within the uppermost 25 km due to the absence of serpentinite in this region (Figures 4a and 4b). Largest deviatoric stresses are *c*. 200 MPa in the uppermost 25 km (Figure 4c). These large deviatoric stresses form a more or less continuous horizontal layer indicating that the entire upper part

of the orogen is under compression (Figure 4c). In contrast, for the 6-km serpentinite model, a weak plate interface made of serpentinite develops in the uppermost 25 km (Figures 4f and 4g). Deviatoric stresses are smaller in the uppermost 25 km of the orogen center, compared to the 3-km serpentinite model (Figure 4g). The different strength of the plate interface in the upper region of the orogen has a strong impact on the syn-convergent exhumation, as will be discussed below. For both the 3- and 6-km serpentinite models, the overall density structure is similar (Figures 4d and 4h), so that differences in density and buoyancy are most likely not causing differences in exhumation dynamics between the two models. In contrast to the simulation with 3-km serpentinite thickness, the simulation with 6-km serpentinite thickness shows syn-convergent exhumation of subducted upper crust, which is also visible by the upwards-bent isotherms associated with thermal advection during exhumation (Figure 4e). In this simulation, the crustal heterogeneities in the distal region of the subducting crust (light blue regions in Figure 4e) have an effective viscosity that is smaller than the one of the surrounding, background crust (blue color in Figure 4e; viscosities shown in Figure 4f) but a density that is larger than the one of the background crust (Figure 4h). The heterogeneities in the more proximal region of the subducting crust (dark blue regions in Figure 4e) have an effective viscosity that is larger compared to the background crust (Figure 4f) and a density that is much larger compared to the background crust (Figure 4h). We refer to these properties of the crustal heterogeneities in the subducting crust as the standard configuration. Since only this simulation with 6-km serpentinite thickness shows significant exhumation, we also investigate the impact of the effective viscosity and density of the crustal heterogeneities on the syn-convergent exhumation (Figure 5).

Figure 5 presents subduction-exhumation dynamics for five simulations with 6-km serpentinite thickness and with varying density and effective viscosity of the heterogeneities in the distal and more proximal regions of the subducting crust (with light and dark blue color). Colorplots of the representative values of densities and effective viscosities are shown in Figures 4f and 4h and Figure S6 in Supporting Information S1. For the simulation with distal heterogeneities (light blue color in Figure 5) having the standard configuration (same simulation as shown in Figures 4e–4h; physical properties are given in Table S1 in Supporting Information S1), syn-convergent exhumation occurs (Figures 5a–5c). If the distal heterogeneities are kept weaker (i.e., standard configuration) but densities are much denser (by employing the densities of the more proximal, dark blue heterogeneities) relative to the background upper crust, then syn-convergent exhumation still occurs (Figures 5d–5f). We observe a similar exhumation style to that of the simulation with standard configuration (Figures 5a–5c). If the distal heterogeneities are kept denser (i.e., standard configuration), but the heterogeneities are made mechanically stronger (by employing the flow law parameters of the more proximal, dark blue heterogeneities), then syn-convergent exhumation also still occurs (Figures 5g–5i). For this simulation, the exhumation style is different since the light blue heterogeneities deform significantly less during subduction and exhumation (Figures 5g–5i). The light blue heterogeneities show a very coherent exhumation and the uppermost exhumed light blue heterogeneity shows the geometry of a fold nappe with an overturned and highly sheared (thinned) limb (Figures 5h and 5i). If the distal heterogeneities are made both much denser and mechanically stronger as the background upper crust, then significant syn-convergent exhumation does not occur anymore for the distal region (Figures 5j–5l). Some exhumation still occurs at the transition between the distal and proximal regions of the subducted crust (dark and light blue heterogeneities in region with upward-bent isotherms in Figure 5l). Finally, if the properties of the distal, light blue heterogeneities with standard configuration are interchanged with the properties of the more proximal, dark blue heterogeneities with standard configuration, then no significant exhumation occurs (Figures 5m–5o). Deformation is localized in the proximal regions with dark blue heterogeneities, which is visible by the strong deformation of these dark blue heterogeneities (Figures 5m–5o). The evolving orogenic wedge without significant exhumation is similar to the thrust-diapir mode of orogenic wedges in the classification of Candioti et al. (2021). The different properties of the distal, light blue heterogeneities also affect the timing of the onset of exhumation (Figures 5a, 5d and 5g). If heterogeneities have standard configuration, then exhumation starts earliest (22 Myr; Figure 5a) and if heterogeneities are stronger and denser, then exhumation starts later (15 Myr; Figure 5g). In the following, we focus on the simulation with standard configuration (Figures 5a–5c) for the comparison between simulations with 3- and 6-km serpentinite thickness.

We use color coding of markers based on their initial paleogeographic position prior to subduction to study their *P-T* trajectories during subduction, collision, and exhumation (Figure 6). We focus on the passive margin of the subducting plate. Furthermore, we analyze representative *P-T* pathways of individual markers (Figure 6). Numerical simulations with a 3-km serpentinite thickness (Figures 6a–6c) subduct continental portions of the distal hyper-extended domain to depths of >100 km. However, these HP domains are unable to exhume to depths

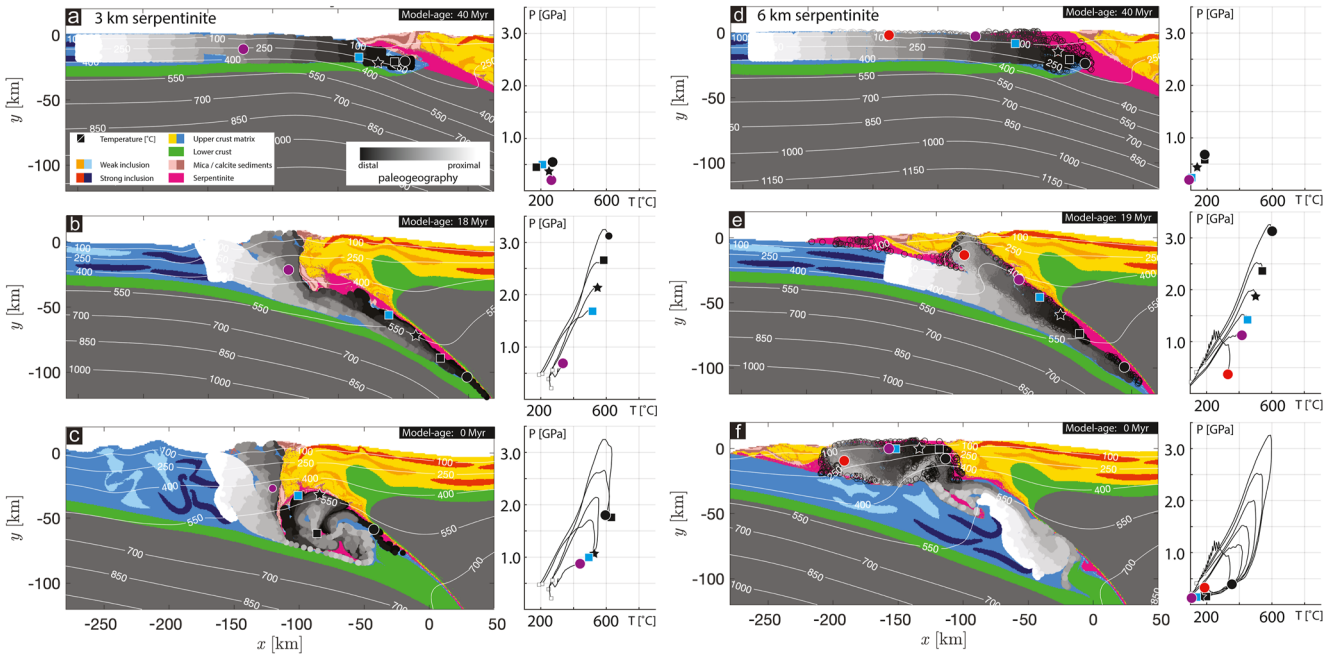

Figure 6. Evolution of model units with markers indicating initial paleogeographic position. (a–c) Model with initially 3-km serpentinite thickness where markers are colored by paleogeographic position at the former hyper-extended margin, as well as representative *P-T* evolution for selected subducted continental particles. Marker colors vary from white (proximal domain) to black (distal domain). (d–f) Model with initially 6-km serpentinite thickness where markers are colored by paleogeographic position at the former hyper-extended margin, as well as representative *P-T* evolution for subducted continental particles.

shallower than 40 km (Figure 6c) and are prevented from reaching the surface by the over-riding plate. These subducted units do not retain their coherency and subsequently form a mechanical mixture below the overriding plate (Figure 6c). The overriding plate also forms a strong buttress to the more proximal domains toward the foreland, preventing them from being subducted (Figures 6a and 6c). The continental collision subsequently initiates foreland-directed folding and thrusting of continental material at shallow depths, as seen by the deformation of the weak and strong heterogeneities within the crust of the subducting plate (Figure 6c). Numerical simulations with a 6-km serpentinite thickness (Figures 6d–6f) also subduct continental portions of the distal hyper-extended domain to depths of >100 km. In contrast to the simulation with 3-km serpentinite thickness, considerable portions of the subducted rocks are exhumed to <5 km depth (Figure 6f). *P-T* trajectories for representative markers within the subducting crust exhibit a clockwise burial and exhumation pathway (Figure 6f). The structural coherency of subducted and exhumed continental portions is maintained. The former paleogeographic transition from distal to proximal can still be observed in the final exhumed configuration, where distal parts are found within the core of the orogeny and proximal portions toward the foreland (Figure 6f). During the early stages of decompression, after peak *P* has been attained, buoyant exhumation of continental markers follows a near-isothermal decompression pathway (Figure 6f).

Figure 7 shows the temporal evolution of pressure, temperature, and depth for individual markers indicated in Figure 6 for both models with 3- and 6-km serpentinite thicknesses. Due to the lack of exhumation of deeply subducted particles for the 3-km serpentinite model, we do not observe notable cooling after peak conditions are attained (Figure 7a). In contrast, for the 6-km serpentinite model we observe cooling during exhumation into the shallower and cooler regions of the lithosphere (Figures 7b and 7d). For both models, we observe that peak values of *P* and *T* do not occur at the same time (Figures 7a and 7b). Typically, peak *T* values post-date peak *P* values with larger discrepancies occurring for models with 3-km serpentinite (Figure 7a). For the 3- and 6-km serpentinite models, the average vertical burial velocities of markers buried deeper than 50 km are *c*. 4.5 mm/yr (Figures 7c and 7d). The average exhumation velocities for the 3-km serpentinite model do not exceed 3 mm/yr (Figure 7c). The exhumation velocities are, hence, slower than the burial velocities. The average exhumation velocities for the 6-km serpentinite model are *c*. 6.5 mm/yr (Figure 7d). However, for short time intervals of few million years, exhumation velocities can exceed 10 mm/yr (e.g., marker indicated by solid black circle between *c*. 9 and 7 Myr in Figure 6d). These exhumation velocities, hence, are larger than subduction-related burial velocities

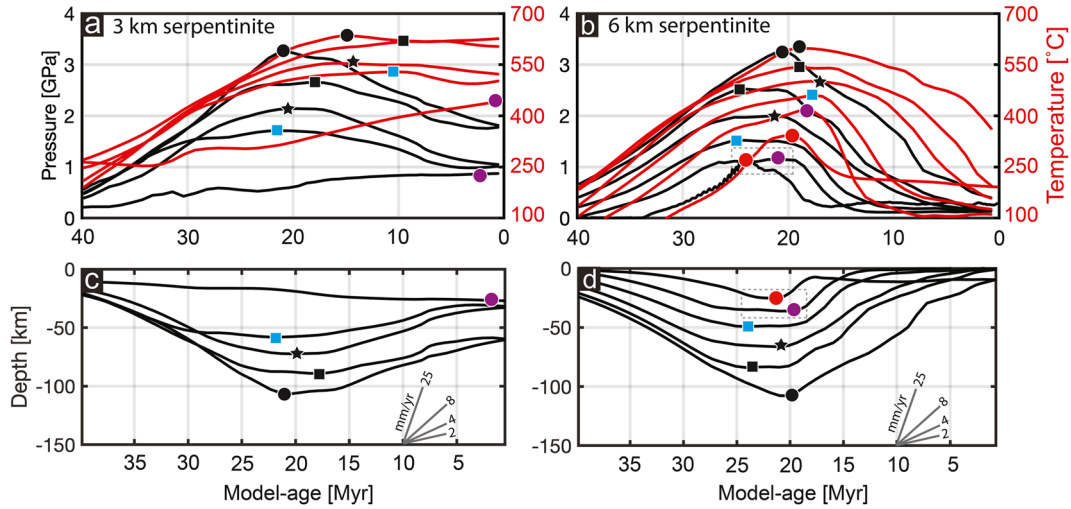

Figure 7. Pressure, temperature, and depth evolution with time of selected markers, whereby marker symbols indicate the conditions of peak metamorphic grade (same markers as those in Figure 6). Left column shows results for models with initially 3-km thick serpentinite and right column results for 6 km. (a and b) *P*-*T*-time evolution with peak temperature and peak pressure conditions indicated. (c and d) Depth-time evolution with maximum depth indicated and representative exhumation velocity gradients. Dashed boxes in panels (b and d) highlight the contribution of tectonic pressure for the red circle marker (see text for details).

(Figure 7d). For one marker of the simulation with 6-km serpentinite, a significant deviation from the lithostatic pressure is observed (red circle marker, Figures 6e and 6f, 7b and Figure S5 in Supporting Information S1). This marker is buried to a maximal depth of *c*. 25 km (Figure 7d). The peak *P* (indicated by the red circle) is similar to the peak *P* of a neighboring marker (indicated by the purple circle), which has been buried *c*. 14 km deeper. The two markers are indicated in the dashed boxes in Figures 7b and 7d, to easily compare their similar peak *P* but different maximal burial depth. For the marker indicated with the red circle (Figures 7b and 7d), the peak *P* is *c*. 0.4 GPa higher with respect to the corresponding lithostatic pressure, indicating a tectonic overpressure (see also Figure S5 in Supporting Information S1).

4.3. Peak Metamorphic Conditions

Peak metamorphic conditions of continental markers that are subducted during convergence are presented in Figure 8. For similar areas within the hyper-extended margin (Figures 6a and 6d), the distribution of peak *P* and *T* conditions for models with 3- and 6-km serpentinite vary considerably (Figure 8). The paleogeographic position of markers prior to subduction also varies for the two models. For 3-km serpentinite, the range of peak *P*-*T* conditions spans a considerable range of pressures; however, the temperature ranges for the corresponding pressure values are more narrow for max. *T* values (Figure 8a), compared to max. *P* values (Figure 8b). The paleogeographic position shows that markers showing lower-grade conditions originate from the more proximal portions of the hyper-extended margin, whereas markers that record high-grade conditions originate from distal regions (Figures 8a and 8b). For the 6-km serpentinite model, the temperature ranges for the corresponding pressure values span a broader temperature range compared to 3-km serpentinite models (Figures 8c and 8d). This temperature range does not vary as considerably between max. *T* (Figure 8c) and max. *P* (Figure 8d) compared to the 3-km serpentinite model. The paleogeographic position correlates stronger with temperature rather than pressure, with more proximal regions reaching higher peak *T* compared to more distal regions (Figures 8c and 8d).

Considering only the markers that are subducted and subsequently exhumed to <25 km depth (red points Figures 8 and 9), we observe a significant difference between models with 3- and 6-km serpentinite: markers for the 3-km serpentinite model do not record $P > 1$ GPa and $T > 400$°C (Figures 9a and 9b), compared to markers for the 6-km serpentinite model that record $P > 3.0$ GPa and $T > 600$°C (Figures 9c and 9d). The majority of ages of peak *P* and *T* for the 3-km serpentinite model occur late in the model evolution (15–5 Myr before the model stops at 0 Myr; Figures 9a and 9b). Peak metamorphic ages for the 6-km serpentinite model based on max. *T* show a trend of older ages (25–5 Myr) compared to the 3-km serpentinite model, where we observe younger ages

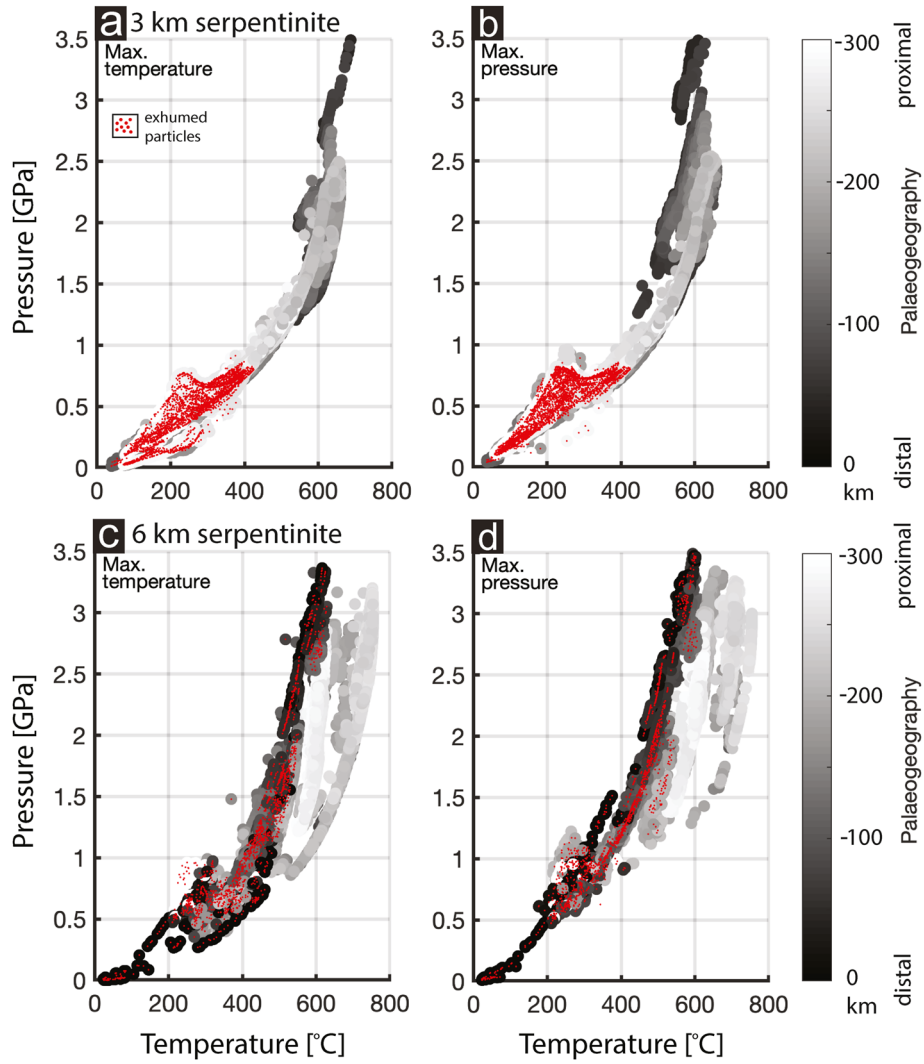

Figure 8. Maximum *P-T* conditions attained by analyzed markers (indicated in white to black colors in Figure 6), colored as function of initial paleogeography within the hyper-extended margin prior to subduction (see Figure 6). Particles exhumed to <25 km depth are indicated in red. Max. temperature (a and c) corresponds to *P-T* conditions determined by using the maximum temperature attained during subduction. Max. pressure (b and d) corresponds to *P-T* conditions determined by using the maximum pressure attained during subduction (see methods in Section 3.3). Top row (a and b) shows results for simulation with initially 3-km thick serpentinite and bottom row (c and d) results for 6 km.

at higher temperatures and lower pressures (e.g., 0.5 GPa and 400°C, Figure 9a). Peak metamorphic ages corresponding to max. *P* values in the 6-km serpentinite model show predominantly older ages (40–5 Myr) compared to max. *T* values (Figure 9c). Ages for max. *T* and max. *P* values exhibit a general trend of older ages for peak metamorphism with increasing temperature (Figure 9d). Furthermore, the results show that the highest peak *T* of exhumed rocks is *c*. 620°C (Figure 9d) and the highest peak *P* is *c*. 3.5 GPa (Figure 9d).

As outlined in Section 3.3, peak metamorphic facies are mapped within the modeled orogen for continental crust that has been subducted and exhumed. This peak metamorphic facies analysis has also been undertaken on 6-km serpentinite simulations where we vary the mechanical properties of the heterogeneities in the upper crust (see Figure S7 in Supporting Information S1). Figures 10a and 10c shows the metamorphic facies distribution for the 3-km serpentinite model based on peak *P-T* values corresponding to max. *T* (Figures 10a and 10b) and max. *P* (Figures 10c and 10d). Overall, the metamorphic facies are distributed in a horizontally layered manner, in cross-section view, across the orogen (Figures 10a and 10c). The majority of subducted markers record eclogite facies and are confined to depths larger than *c*. 40 km. Minor volumes of UHP facies are present in the deeper

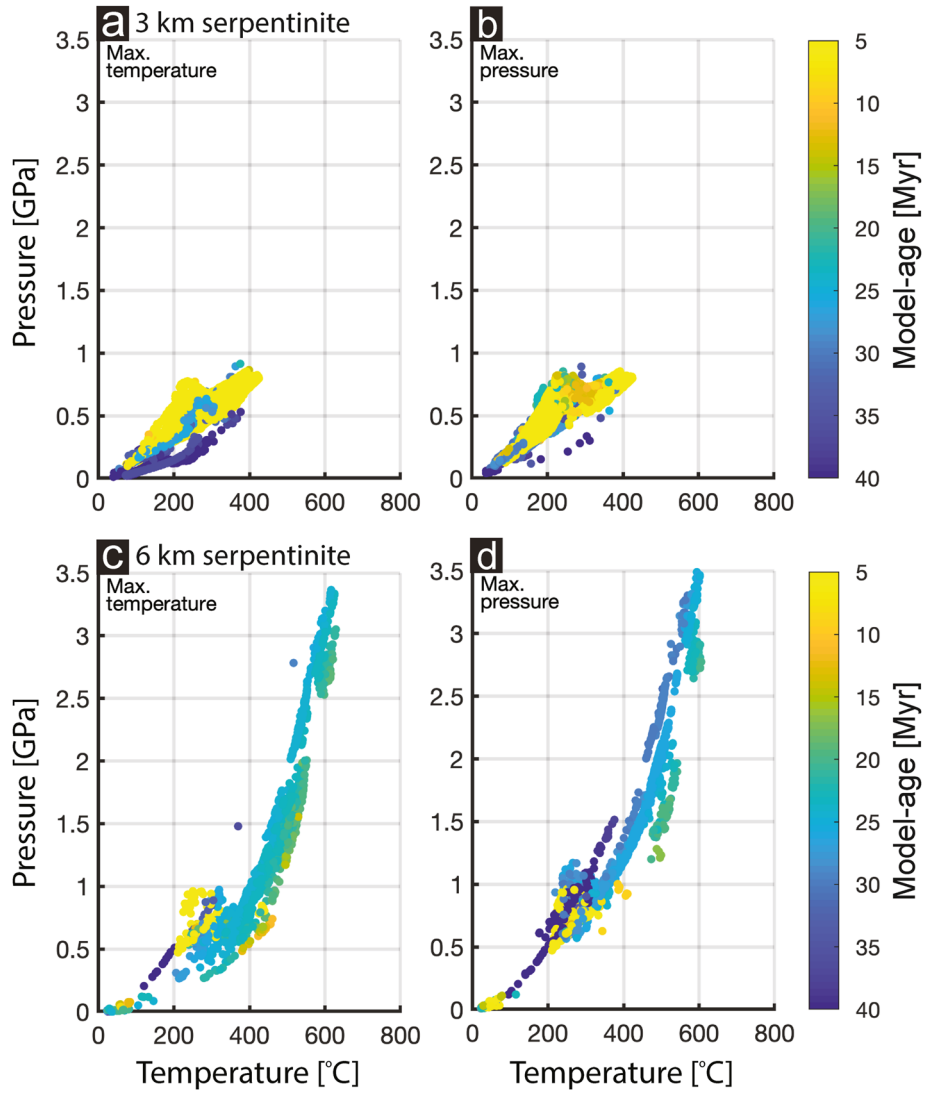

Figure 9. Age of maximum *P-T* conditions attained by particles subducted and exhumed to <25 km depth, colored as a function of age of peak metamorphic conditions. Top row (a and b) shows results for simulation with initially 3-km thick serpentinite and bottom row (c and d) results for 6 km. Max. temperature corresponds to *P-T* conditions determined by using the maximum temperature attained during subduction. Max. pressure corresponds to *P-T* conditions determined by using the maximum pressure attained during subduction (see methods in Section 3.3).

portions of the orogen where substantial tectonic mixing has occurred (*c*. 40 km; Figures 10a and 10b). Higher volumes of blueschist and UHP facies are present for peak conditions based on max. *P* values (Figures 10c and 10d), than compared to max. *T* (Figures 10a and 10b). Figures 10e and 10g shows the metamorphic facies distribution for the 6-km serpentinite model. Overall, metamorphic facies of continental regions exhumed to depths <25 km are distributed laterally across the orogen. The highest grades are observed within the core of the orogen closer to the upper plate and decrease in grade toward the foreland (Figures 10e and 10g). For peak metamorphic values based on max. *T*, metamorphic grades ranging from UHP, eclogite, blueschist, greenschist, and zeolite are observed within the uppermost 25 km (Figure 10e). Similar to the 3-km serpentinite model, the 6-km serpentinite model also contains relatively larger volumes of UHP and blueschist facies for peak conditions based on max. *P* values (Figures 10g and 10d), compared to max. *T* (Figures 10e and 10f). High-temperature amphibolite facies occur in small volumes between 30 and 40 km depth for max. *T*-based facies models (Figure 10e), something that is not observed in max. *P*-based facies models (Figure 10g).

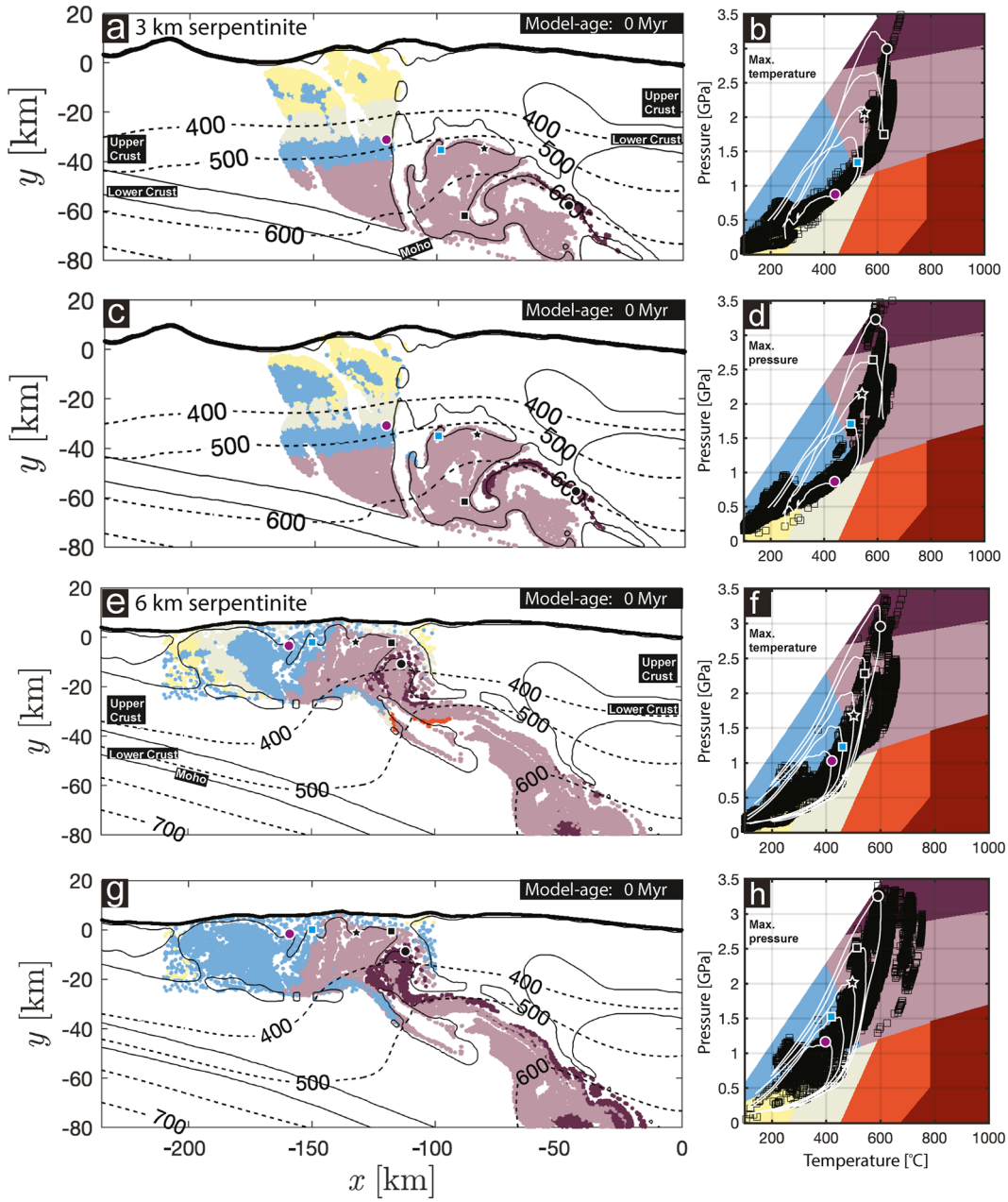

Figure 10. (a) Numerically calculated metamorphic facies distribution for the model with initially 3-km serpentinite thickness, based on max. temperature. (b) Representative maximum *P-T* conditions plotted over metamorphic facies grid (black squares; modified after Philpotts and Ague (2009)) and representative *P-T* loops (similar to markers in Figures 6 and 7 where peak conditions are indicated by colored markers). (c) Metamorphic facies distribution (3-km serpentinite model) based on max. pressure. (d) Representative maximum *P-T* conditions plotted over metamorphic facies grid (black squares) and representative *P-T* loops (similar to markers in Figures 6 and 7 where peak conditions are indicated by colored markers). (e) Metamorphic facies distribution (6-km serpentinite model) based on max. temperature. (f) Representative maximum *P-T* conditions plotted over metamorphic facies grid (black squares) and representative *P-T* loops (similar to markers in Figures 6 and 7 where peak conditions are indicated by colored markers). (g) Metamorphic facies distribution (6-km serpentinite model) based on max. pressure. (h) Representative maximum *P-T* conditions plotted over metamorphic facies grid (black squares) and representative *P-T* loops (similar to markers in Figures 6 and 7 where peak conditions are indicated by colored markers).

5. Discussion

5.1. Serpentinite Thickness and Subduction Interface Strength

The variation in initial thickness of serpentinized exhumed mantle (here 3 or 6 km), separating the hyper-extended passive margins formed during rifting, has a dramatic effect on the subduction and exhumation style in the modeled orogens. In our models, the weak serpentinite is the main model feature that controls the strength of the emerging subduction interface. Where serpentinite is present and numerically resolvable along the subduction interface, there the interface is weak. Where serpentinite is missing, or numerically not resolvable, there the interface is strong (Figure 4). In nature, the emerging subduction interface strength is likely also controlled by more complex processes such as fluid-induced softening, reaction-induced softening, partial melting, grain size reduction, or anisotropy development. These microscale and multiphase processes are currently not considered in our large-scale lithosphere-upper mantle model. Therefore, the presence and distribution of serpentinite along the emerging subduction interface is a proxy for the subduction interface strength. In our model, an initial serpentinite thickness of 6 km is required so that a subduction interface with a layer of sheared serpentinite can develop and be numerically resolved. A layer of 6-km thick serpentinite is larger than typically observed thicknesses of serpentinites above exhumed mantle, such as in the exhumed units from the former Piemonte-Liguria domain (McCarthy et al., 2020). However, serpentinized peridotite has been suggested to reach depths of 8 km, which is also supported by geophysical evidence (Andréani et al., 2007; Chian et al., 1999; McCarthy et al., 2020). The main reason for including a potentially too large initial serpentinite thickness in our model is due to the numerical resolution of 1×1 km. In order to form a numerically resolvable layer of serpentinite after significant shearing and thinning during subduction, an initial thickness of 6 km is required in our model. Consequently, the applied initial thickness of serpentinite should be considered with caution when compared directly with typical natural thicknesses of serpentinite.

5.2. Impact of Density and Strength of Crustal Heterogeneities

Including initially elliptical mechanical heterogeneities throughout the upper regions of the model lithosphere (Figure S1 in Supporting Information S1) is motivated by field observations in the Central and Western Alps, which indicate a mechanically heterogenous preconvergence lithosphere (Duretz et al., 2016; Petri et al., 2019). Systematic studies by Duretz et al. (2016) and Petri et al. (2019) highlight the influence of mechanical heterogeneities during passive margin formation. These numerical studies show that mechanical heterogeneities can generate a variety of features which are observed in exhumed portions of the former Alpine passive margins, such as extraction faults, metamorphic pressure jumps, high-angle and low-angle normal faults, anastomosing shear zones, and decoupling horizons. Simulations with mechanical heterogeneities of orogenic wedge formation were also performed by Candioti et al. (2021).

During the extension simulation, the weak elliptical heterogeneities have been deformed during passive margin formation (Figure 3). Hence, the heterogeneities in the distal region of the passive margin that will eventually subduct (light blue heterogeneities) have a more complex geometry before the onset of crustal subduction (Figure 3d). We show, with simulations having 6-km serpentinite thickness, that the style and timing of syn-convergent exhumation is affected by the density and mechanical strength of the heterogeneities in the subducted upper crust (Figure 5 and Figure S6 in Supporting Information S1).

The simulation with weak distal heterogeneities having densities of *c*. 3,300 kgm^{-3} (Figures 5d–5f and Figure S6b in Supporting Information S1) shows that these very dense rock units are exhumed during ongoing convergence (Figure S6b in Supporting Information S1). Hence, this simulation can explain the exhumation of smaller volumes of denser rocks (e.g., eclogite facies rocks) together with larger volumes of less dense rocks, which has been already suggested by previous studies (e.g., Burov et al., 2014; England & Holland, 1979) but was not shown with numerically highly resolved crustal heterogeneities as presented here. Furthermore, distal heterogeneities that are mechanically stronger as the background crust exhume as structurally coherent units and can form structures resembling fold nappes with a thinned and stretched overturned limb (Figures 5h, 5i and Figure S6c in Supporting Information S1). If the distal heterogeneities are both stronger and much denser than the background crust, then significant syn-convergent exhumation of the distal crustal units does not occur (Figures 5j–5l, Figures S6g and S6e in Supporting Information S1), likely because for this scenario, shear forces and resisting

exhumation are larger than buoyancy forces. The interplay between buoyancy versus shear forces during orogenic wedge formation has been studied in more detail in Candioti et al. (2021).

5.3. Syn-Convergent Exhumation, Local Extension, and Normal-Sense Shear Zones

Published syn-convergent exhumation models (e.g., Butler et al., 2014) have been criticized because they often require significant erosion, which is not observed in the Western Alps in several regions within proximity to exhumed (U)HP terranes (e.g., Liao et al., 2018; Malusà et al., 2015). In our syn-convergent exhumation model with a weak subduction interface (6-km serpentinite thickness), significant erosion is not required (Figures 5, 6 and 11). The low-viscosity serpentinites form a weak subduction interface in the uppermost 25 km (Figures 4e and 4f and 5). The upper crust of the upper plate can, therefore, easily thrust above the lower plate toward the foreland. The subducted buoyant crust of the lower plate pushes upward and causes the upper plate to neck, or to boudinage, and to ultimately separate (Figure 11). This necking and lateral separation indicates local upper plate extension. During this local extension, the separated upper plate rocks move toward the foreland, which is possible due to the weak interface below the separated unit. This separation enables the subducted rocks from the lower plate to exhume to the surface (Figures 5a–5i and 11a–11c).

Another feature of our syn-convergent exhumation model is a prominent shear zone with a normal shear sense (Figure 11). To visualize the shear sense, an initially rectangular box, whose long axis is parallel to the subduction interface, is plotted using four numerical markers that define the corners of the rectangle (Figure 11a). During subduction, the box is progressively sheared with a normal sense of shear as the material below the subduction interface is being exhumed (Figures 11b–11d). The sides of the initial rectangle parallel to the subduction interface remain at fixed distances during progressive exhumation, attesting to the coherency of the exhuming material (Figures 11c and 11d). The sides of the initial rectangle perpendicular to and across the subduction interface are significantly extended (Figure 11d). Using the deformed box as a shear sense indicator, we observe local normal sense (extensional) shear between the overriding plate and the exhuming continental units. Our results show that local extension and crustal boudinage, as well as the formation of large-offset, crustal-scale shear zones with normal sense, can occur during continuous plate convergence.

The model with a strong subduction interface (3-km serpentinite thickness) does not show significant exhumation. The absence of exhumation is largely due to the behavior of the overriding plate (Figures 4a–4c). The overriding plate acts like a strong lid and prevents HP units from exhuming to the surface. Local extension of the upper plate is inhibited, due to the lack of a weak plate interface in the uppermost 25 km and the collision of the upper crusts of the two passive margins (Figures 4a and 4b).

5.4. Predictive Modeling of Metamorphic Facies

Our results indicate that using the peak P and T, incurred by markers during their clockwise P-T path, is a good approximation for the distribution of subduction-related metamorphic facies (Figure 10). The assumptions made here with regard to "freezing" in time the peak metamorphic grades, expressed in petrology as assemblages (Section 3.3), do not differ considerably from the assumptions made when applying geo-thermobarometers to natural samples. These assumptions are mainly, (a) equilibrium conditions in pseudo-section calculations, (b) equilibrium due to water presence or water saturated conditions, (c) peak metamorphic conditions can be identified with textural observations, and (d) kinetics can be neglected. Questions arising from the assumption that the relative phases in a peak assemblage equilibrated at a single P-T condition are not evaluated in this study (e.g., Spear, 1989; Spear et al., 2017). Such factors as the kinetics of metamorphic reactions during prograde pathways focus on the scale of the mineral, whereas peak metamorphic conditions applied to the entire orogeny focus on regional-scale trends (Figure 2). Considerable effort has been made to map such large-scale subduction-related metamorphic trends throughout the Western Alps (e.g., Agard et al., 2002; Babist et al., 2006; Beltrando, Compagnoni, & Lombardo, 2010; Berger & Bousquet, 2008; Bousquet et al., 2008; Oberhänsli et al., 2004), and these trends primarily focus on peak P and T conditions. Therefore, we find the application of our simplified metamorphic facies model to regional metamorphic facies distributions observed in natural orogens justified.

Differences in the metamorphic architecture of the modeled orogeny arise when using max. P or max. T values for defining the metamorphic facies in P-T space (Figure 10 and Figure S5 in Supporting Information S1). Although the larger-scale metamorphic structure is consistent, occurrences of blueschist facies and UHP facies

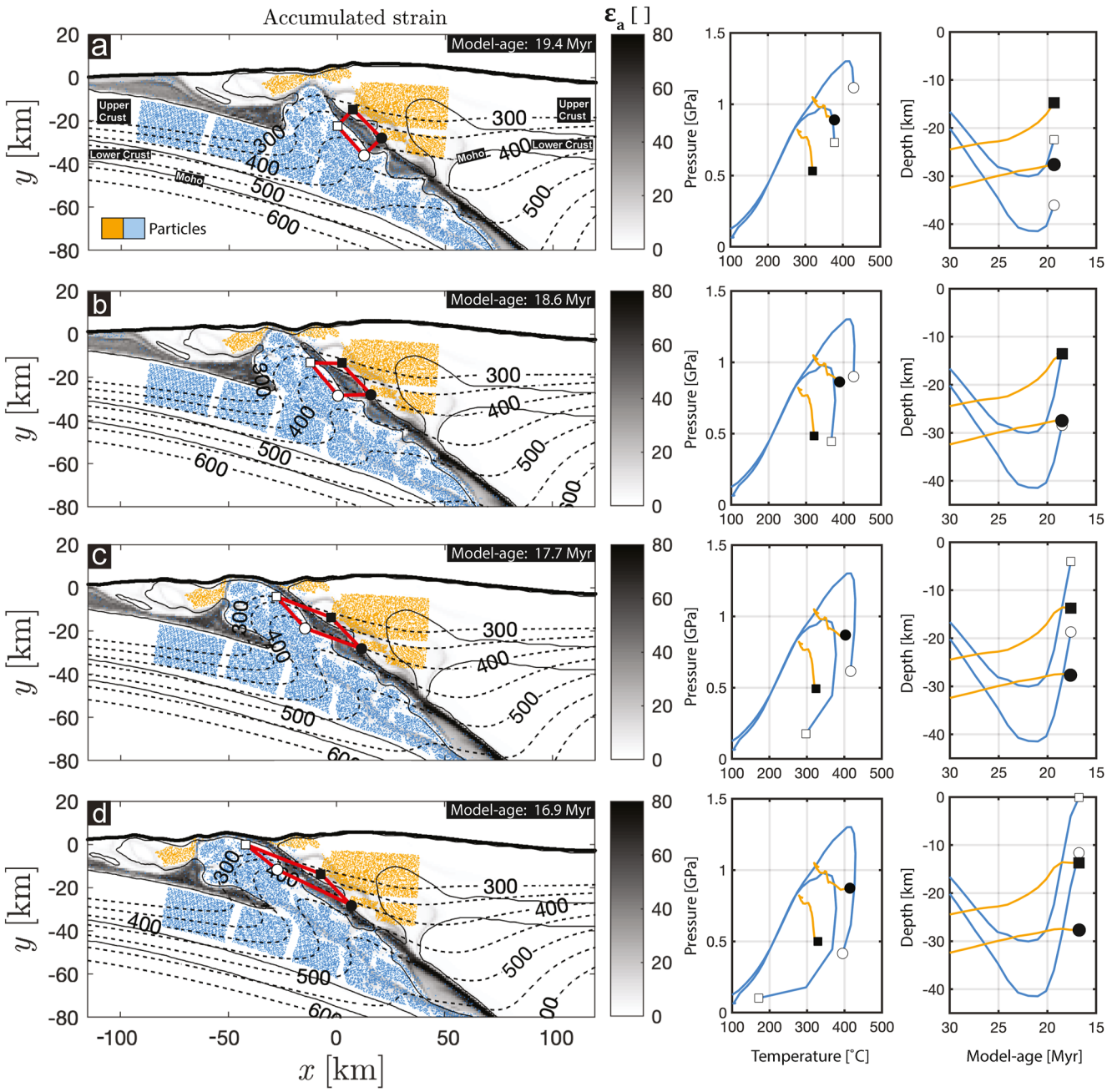

Figure 11. Evolution of accumulated strain (ε_a [ ] is the time integral of the strain rate invariant at each numerical grid point and is dimensionless, where white colors indicate low strain and dark colors high strain) with pressure-temperature paths and depth-time paths for four selected markers that form the red parallelogram in the leftmost panels. Selected markers from overriding plate are yellow and markers from subducting plate are blue to visualize exhumation and lateral separation of upper plate during local extension. Dashed black lines indicate isotherms and numbers on dashed lines indicate temperature in °C. Rows (a–d) show results for four different model ages. Results are from the model with initially 6-km serpentinite thickness. The four corners of the red parallelogram are defined by markers whereby the two black markers are from the upper plate and the two white markers are from the subducting plate. The progressive shear deformation of the red parallelogram during exhumation indicates a normal-type shear sense between exhuming units and upper plate.

P-T conditions are more widespread in both 3- and 6-km serpentinite models when using max. *P* (Figures 10c and 10g). This is primarily due to peak *P* and *T* values not being consistent (Figure S5 in Supporting Information S1), for example, where a decrease in *P* occurs during continued heating. Peak *T* can be between 50°C and 100°C hotter than the corresponding *T* at peak *P* (e.g., red circle marker, Figures 6e, 6f and 7b). The observed increase in blueschist and UHP facies occurrences for max. *P* values likely reflects the pressure dependent slope

of the lower boundaries of metamorphic facies in *P-T* space (Figure 2b). This *P* dependency is exemplified if we consider what facies are being replaced by blueschist and UHP facies when considering max. *P*. Typically, blueschist facies replaces greenschist facies, and UHP facies replaces HP facies (Figures 10e and 10g). Therefore, the use of metamorphic facies in our models indicates relative *P-T* conditions (Ghent, 2020).

5.5. Deviations From Lithostatic Pressure

The rock pressure cannot strictly be lithostatic, or hydrostatic, everywhere within the crust during orogeny, because plate driving forces, rock deformation, and lateral topography variations are caused by differential stresses (e.g., Schmalholz et al., 2014, 2019; Turcotte & Schubert, 2002). The magnitude of the deviation of rock pressure from lithostatic pressure during orogeny is disputed. Several studies suggest that some observed metamorphic rock units indicate pressures that deviate significantly from the lithostatic pressure, say deviations >0.2 GPa (e.g., Jamtveit et al., 2018; Luisier et al., 2019; Putnis et al., 2021; Vaughan-Hammon et al., 2021b). These potential deviations from lithostatic pressure, so-called tectonic pressure (e.g., Gerya, 2015; Moulas et al., 2013; N. S. Mancktelow, 2008; Petrini & Podladchikov, 2000; Schmalholz & Podladchikov, 2013), are commonly proposed for smaller units, such as lenses or shear zones, typically having a size of less than 100 m. Our model cannot resolve such small scale units, which usually are interpreted to have significantly different strength than the surrounding rocks. However, one region of the syn-convergent exhumation model presented (the red circle in Figure 6 shows a representative marker) shows a deviation from lithostatic pressure of *c*. 0.4 GPa. A representative numerical marker of this region belongs to portions of the background (i.e., not an elliptical heterogeneity) continental crust, which builds up significant differential stress during subduction. This differential stress and associated tectonic pressure is the result of the mechanically heterogeneous precollisional continental lithosphere, due to weak and strong ellipses, which is motivated by field studies in the Western Alps (Petri et al., 2019). Several studies suggest such deviations from the lithostatic pressure in the order of a few hundreds of MPa, based on the metamorphic rock record in the Monte Rosa unit (Luisier et al., 2019, 2021; Vaughan-Hammon et al., 2021a, 2021b). Furthermore, some studies propose that deviations from lithostatic pressure can also be caused by differential volumetric deformation, for example, due to dehydration reactions (Luisier et al., 2019, 2021; Schmalholz et al., 2020; Vaughan-Hammon et al., 2021a). Such volumetric changes are not considered in our model assuming incompressible deformation. Therefore, due to the applied numerical resolution of 1 × 1 km and the assumption of incompressible deformation, our model results are not suitable to study potential deviations from lithostatic pressure occurring on spatial scales of less than 1 km.

5.6. Application to the Western Alps

For the model with a strong subduction interface (3-km serpentinite thickness; Figures 10a and 10c), the magnitudes of peak metamorphic grades are in agreement with exhumed (U)HP units observed in the Western Alps (Figures 10b and 10d). However, for this model, the rocks with (U)HP facies remain at depths of >40 km and do not exhume close to the surface. The absence of significant exhumation is evident in the horizontally layered metamorphic architecture (Figures 10a and 10c) as well as the absence of closed clockwise *P-T* loops (Figures 10b and 10d). Therefore, the model with a strong subduction interface is not applicable to the Western Alps, mainly due to the lack of exhumation of (U)HP units. The resulting metamorphic architecture for the model with a weak subduction interface (6-km serpentinite) and syn-convergent exhumation agrees to first order with the metamorphic facies distribution in the Western Alps (Figures 2, 10 and 12). In the Western Alps, high-grade internal metamorphic zoning exists showing a decrease in grade toward the foreland (e.g., Ernst, 1972). The same trend exists in the modeled metamorphic facies distribution (Figure 12). However, more external (also lower grade) domains in the Alps (e.g., Aar massif) are observed to have horizontal (or doming) peak metamorphic zoning patterns (e.g., Nibourel et al., 2021). Hence, the younger, postcollisional deformation in the external Alps might be closer to our models with strong subduction interface, which resemble the formation of a fold-and-thrust wedge (Figures 4a and 4b). The metamorphic facies gradient from high to low grade also predicts the subduction polarity (Ernst, 1971, 1972), whereby the direction of increasing grade is the direction of lower-plate subduction (Figure 12). The metamorphic facies distribution, hence, preserves, or "fossilizes," the subduction-related metamorphic architecture that was formerly at greater depths. Serpentinites control (to some extent) this "fossilization" process by aiding exhumation of (U)HP units to the surface via buoyancy and lubrication of a low-viscosity subduction interface. The widespread occurrences of serpentinites associated with

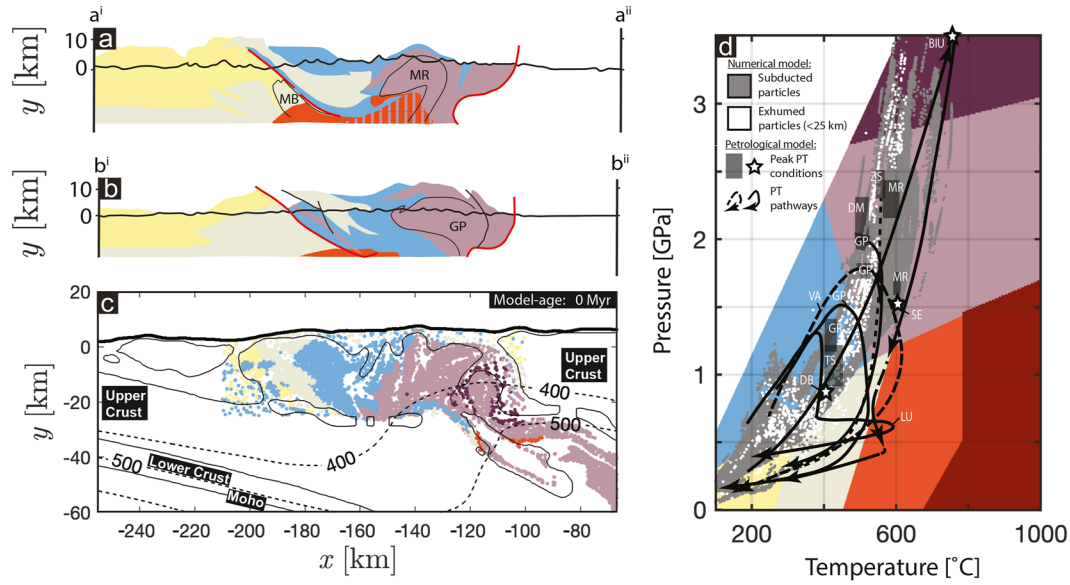

Figure 12. Comparison of observed metamorphic facies distribution (in cross-section view) with numerically calculated metamorphic facies. (a and b) Simplified cross sections of observed metamorphic facies distributions of the Western Alps (modified after Oberhänsli et al. (2004) and Bousquet et al. (2008); see Figure 2 for location of the two cross sections). (c) Numerically calculated metamorphic facies distribution (based on maximum temperature) for model with initially 6-km serpentinite thickness. (d) *P-T* metamorphic facies grid (modified after Philpotts & Ague, 2009) comparing peak numerical *P-T* values for all markers (colored in gray) and exhumed markers (colored in white) with representative *P-T* estimates for major Western Alpine units (references and abbreviations are given in Figure 2). The vertical and horizontal scales for the cross sections in panel (a–c) are identical.

HP domains within the Western Alps, for example, the Zermatt-Saas ophiolite (e.g., Forster et al., 2004), could indicate their involvement in exhumation processes (Agard et al., 2018; Chang et al., 2009; Guillot et al., 2015; Ruh et al., 2015; Schwartz et al., 2001; Yang et al., 2020).

The differences between the two models with strong (Figure 4a) and weak (Figure 4e) interfaces in the modeled metamorphic architecture arise due to two contrasting styles of orogeny: (a) pure wedge-like thrusting associated with horizontally layered metamorphic zoning for a strong interface (Figures 4a and 10a), and (b) wedge formation involving syn-convergent exhumation associated with vertically layered metamorphic zoning for a weak interface (Figures 4e, 5a–5i and 10e). The two numerical models presented here are end-member representations of metamorphic facies development, whereas in nature, and specifically the Alps, a combination of these endmembers likely generated many natural orogens. The impact of serpentinite strength, upper crustal strength, and buoyancy on the style of orogenic wedge formation has also been investigated by Candioti et al. (2021).

Inherited structural complexity deriving from extensional tectonics within the former passive margin (Figure 1a) may also contribute to the structurally complex and minor volumes of exhumed coherent UHP units observed throughout the Western Alps, for example, Brossasco-Isasca unit (BIU; peak *P* is *c*. 3.5–4.0 GPa and peak *T* is *c*. 700°C–750°C) within the Dora Maira massif (Figure 2; e.g., Bonnet et al., 2022; Groppo et al., 2019; Rubatto & Hermann, 2001). In our models with a weak interface, there are subducted and exhumed units that have peak *P-T* values similar to the ones of most units of the Dora Maira massif (2–2.4 GPa and 500°C–540°C: Bonnet et al., 2022; Groppo et al., 2019). However, the UHP and high-*T* markers similar to values for the BIU are not exhumed (Figure 12d), but the largest peak *P-T* values of rocks exhumed in our model (3.5 GPa and 620°C) are quite close to peak values of the BIU. The BIU is a very small tectonic slice (*c*. 1 km thickness) and our model cannot resolve such small units and shear zones around such small units due to the numerical resolution of 1 × 1 km. Also, the BIU might have been an individual extensional allochthon, structurally separated from the main distal passive margin (e.g., Bonnet et al., 2022). Such extensional allochthonous are also not included in our preconvergence model configuration (Figure 3b). In nature, the BIU might have been exhumed as a small individual slice, but the exhumation mechanism remains disputed. Simple numerical models have shown that significant

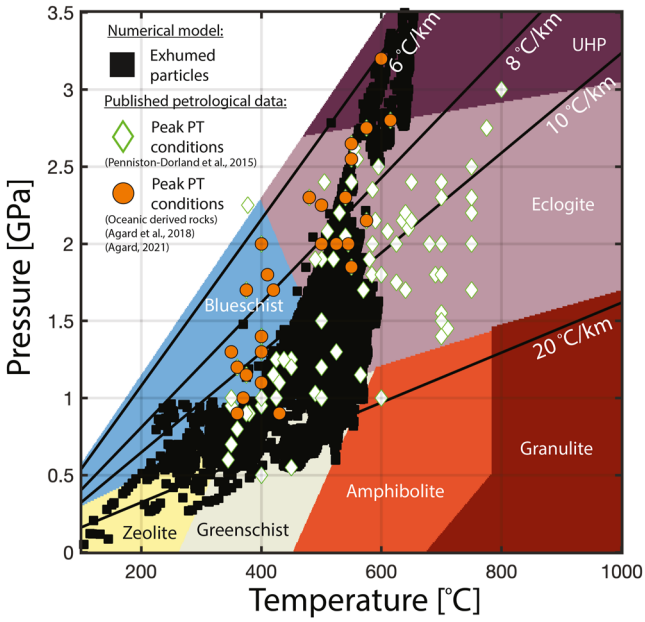

Figure 13. Comparison of peak metamorphic conditions of crustal material exhumed during syn-convergent exhumation for three simulations with 6-km serpentinite thickness (black squares, from models shown in Figures 5a–5i) with published estimates of peak metamorphism for a variety of natural rocks throughout the Alps (Agard, 2021; Agard et al., 2018; Penniston-Dorland et al., 2015). Metamorphic facies grid modified after Philpotts and Ague (2009).

strain localization around the BIU might have enabled diapiric exhumation of the BIU as an individual slice along the subduction interface after its detachment from the subducting plate (Schmalholz & Schenker, 2016).

Progressive exhumation of HP footwall material along a major normal sense shear zone has been suggested for several regions throughout the Alps (Beltrando, Lister, et al., 2010; Bucher et al., 2003; Campani, Herman, & Mancktelow, 2010; Campani, Mancktelow, et al., 2010; Cawood & Platt, 2020; Manzotti, Zucali, et al., 2014; N. Mancktelow, 1985; S. Reddy et al., 1999; S. M. Reddy et al., 2003; Ring & Merle, 1992; Wheeler et al., 2001). Although shear sense indicators are documented, the actual mechanism for generating such normal sense structural features is still unclear (e.g., Bucher et al., 2003). Two scenarios are possible: (a) periods of intermittent far-field plate divergence between periods of convergence (e.g., Beltrando, Lister, et al., 2010; S. Reddy et al., 1999), or (b) exhumation and extrusion of subducted material during continuous plate convergence (e.g., Butler et al., 2014; Chemenda et al., 1995; Duretz et al., 2012; Froitzheim et al., 2006, 2003; Keller et al., 2005). Our model results for syn-convergent exhumation agree with shear sense indicators resulting from extrusion of subducted material (e.g., Chemenda et al., 1995; Duretz et al., 2012; Froitzheim et al., 2006, 2003; Keller et al., 2005; Figure 11). This model also shows the separation of the upper plate crust during exhumation (Figures 11c and 11d, yellow particles). Such separation of the Adriatic upper plate could explain the far-traveled Adria-derived units within the external domains of the Western Alps, such as the Gets and Simme nappes, which have been correlated to the Adriatic passive margin (Figure 1; Escher et al., 1997; Ferrando et al., 2004; Gasinski et al., 1997).

Estimated exhumation velocities for some exhumed continental (U)HP units in the Western Alps indicate that exhumation velocities are approximately equal to or larger than burial velocities (e.g., Agard et al., 2009; Manzotti et al., 2018; Rubatto & Hermann, 2001). In our syn-convergent exhumation model, the fastest burial velocities are *c*. 4.5 mm/yr and average exhumation velocities are 6.5 mm/yr (Figure 7d), sometimes exceeding 10 mm/yr (Figure 7d). Our syn-convergent exhumation model, therefore, agrees with estimated exhumation velocities for major tectonic units of the Western Alps (e.g., Agard et al., 2009; Manzotti et al., 2018).

We compare all peak *P* and *T* data of exhumed rocks from our three simulations with significant syn-convergent exhumation (simulations shown in Figures 5a–5i) with two data sets (Agard, 2021; Agard et al., 2018; Penniston-Dorland et al., 2015) of peak *P* and *T* values from the Alps, which were estimated from natural rocks (Figure 13). The data from Penniston-Dorland et al. (2015) include data from the entire Alps, including oceanic and continental rocks, whereas the data from Agard et al. (2018) and Agard (2021) include only data from oceanic rocks. Overall, our modeled peak *P* and *T* values are well within the wide range of peak *P* and *T* estimates from natural rock (Figure 13). In the peak *P* range between 1.5 and 2.5 GPa, our modeled data provide peak *T* values of maximal 600°C while estimates from natural rocks include peak values of up to 750°C (Figure 13). Peak *T* estimates from natural rocks vary widely between 500°C and 750°C for corresponding peak *P* values in the range of 1.5–2.5 GPa. This wide range of peak *T* estimates for natural rocks, especially peak *T* estimates >600°C, suggests considerably variable thermal conditions in both space and time within the Alpine belt, which could be related to processes not considered in our models, such as magmatism, exothermic hydration reactions, and advective heat transport associated with fluid flow.

In summary, our model of syn-convergent exhumation agrees with the following eight tectono-metamorphic features, observations, and data from the Western Alps: (a) regional-scale structurally coherent units with the same metamorphic facies (Figures 2 and 12), (b) a continuous metamorphic facies gradient with the highest grades in the internal domain and lowest grades in the external domain (Figures 2 and 12), (c) modeled *P-T-t* paths that agree with estimated *P-T-t* paths for representative volumes of major tectonic units, such as the Dora Maira massif (Figure 12), (d) exhumed rock units with a range of peak *P* and *T* values that lie within the wide

range of estimated peak *P* and *T* values from natural rocks in the Alps (Figure 13), (e) exhumation without significant erosion, visible by the essentially constant area of crustal model units (Figures 5 and 11), (f) normal shear sense observed in the upper regions of some exhumed units (Figure 11), (g) remnants of tectonic units originating from the Adriatic margin, which are found in the external domain of the Western Alps (e.g., Simme and Gets nappes; Figures 1, 5 and 11), and (h) exhumation velocities that are larger than the burial velocities (Figure 7).

6. Conclusions

We show with a petrological-thermomechanical numerical model that syn-convergent exhumation of UHP rocks at a subduction zone can occur without significant erosion. In our model, we do not predefine the location of subduction initiation, the geometry of the subduction zone, or the strength of the subduction interface; syn-convergent exhumation develops spontaneously. Syn-convergent exhumation is enabled by a weak subduction interface in combination with local upper-plate extension, which occurs during continuous subduction and plate convergence. In our model, the initial thickness of serpentinites, before convergence and subduction initiation, represents a proxy for the strength of the subsequently developing subduction interface. A weak interface (here for 6-km initial serpentinite thickness) enables significant burial and exhumation of crustal units, while a strong interface (here for 3-km thickness) inhibits exhumation to the surface. The strength of the subduction interface has, therefore, a major impact on the orogenic style: an orogenic wedge with syn-convergent, extrusion-type exhumation develops with a weaker interface, and an orogenic wedge dominated by thrust-type nappe stacking develops without significant exhumation with a stronger interface.

The applied model calculates the metamorphic facies evolution and distribution during orogenesis with approximately 10,000 numerical markers recording peak temperature and pressure. For a strong subduction interface without significant exhumation, the metamorphic facies varies mainly in the vertical direction. In contrast, for syn-convergent exhumation, the resulting metamorphic facies varies mainly in the horizontal direction and shows two main characteristics: (a) exhumed, structurally coherent regions with the same metamorphic facies, which indicate the absence of significant mechanical mixing, or tectonic mélange, and (b) a facies distribution which shows a transition from eclogite to blueschist to greenschist facies when going from the internal to the external (toward foreland) domains.

The modeled structural coherency and the facies distribution agree, to first order, with observations in the Western Alps. Also, the modeled pressure-temperature-time paths, as well as minor erosion in the models and modeled exhumation velocities that are larger than burial velocities, largely agree with representative data from the Western Alps. Furthermore, the modeled orogenic wedge exhibits far-traveled units from the overriding plate in the external domains, which also agrees with natural observations of far-traveled Adria-side units within the external domains of the Western Alps, such as the Gets and Simme nappes. Moreover, the simulations show that a crustal-scale shear zone with normal sense forms during syn-convergent exhumation and that smaller rock volumes with mantle densities can exhume together with larger rock volumes having typical crustal densities, which are also two features relevant for the Western Alps. Based on our results, we conclude that syn-convergent exhumation is a physically feasible mechanism for exhumation of UHP units in the Western Alps, and likely in other orogens worldwide.

We propose that future numerical modeling studies of orogeny should also generate metamorphic facies distributions, because the comparison of modeled and natural facies distributions represents a useful test for the applicability of numerical models to specific natural orogens.

Data Availability Statement

All data relevant for this study are available on the general-purpose open-access repository Zenodo (https://zenodo.org/record/6619759%23.Yp9FsuxBzcw).

Acknowledgments
The authors thank Philippe Agard and one anonymous reviewer for their constructive and useful reviews as well as Editor Whitney Behr and an Associate Editor for editorial handling. This work was supported by the Swiss National Science Foundation Grant Nos. 200021-165756 and 200020-163169. J. D. Vaughan-Hammon thanks Lukas Baumgartner, Evangelos Moulas, and Philip Groß for helpful discussions. S. M. Schmalholz thanks Jean-Luc Epard for many enlightening discussions on Alpine tectonics and for providing information concerning the Simme and Gets nappes. The authors dedicate this study to the late Albrecht Steck.

References

Agard, P. (2021). Subduction of oceanic lithosphere in the Alps: Selective and archetypal from (slow-spreading) oceans. *Earth-Science Reviews*, *214*, 103517. https://doi.org/10.1016/j.earscirev.2021.103517

Agard, P., Monié, P., Jolivet, L., & Goffé, B. (2002). Exhumation of the Schistes Lustrés complex: In situ laser probe $^{40}Ar/^{39}Ar$ constraints and implications for the Western Alps. *Journal of Metamorphic Geology*, *20*(6), 599–618. https://doi.org/10.1046/j.1525-1314.2002.00391.x

Agard, P., Plunder, A., Angiboust, S., Bonnet, G., & Ruh, J. (2018). The subduction plate interface: Rock record and mechanical coupling (from long to short timescales). *Lithos*, *320*, 537–566. https://doi.org/10.1016/j.lithos.2018.09.029

Agard, P., Yamato, P., Jolivet, L., & Burov, E. (2009). Exhumation of oceanic blueschists and eclogites in subduction zones: Timing and mechanisms. *Earth-Science Reviews*, *92*(1–2), 53–79. https://doi.org/10.1016/j.earscirev.2008.11.002

Amiguet, E., Van De Moortèle, B., Cordier, P., Hilairet, N., & Reynard, B. (2014). Deformation mechanisms and rheology of serpentines in experiments and in nature. *Journal of Geophysical Research: Solid Earth*, *119*(6), 4640–4655. https://doi.org/10.1002/2013jb010791

Andréani, M., Mével, C., Boullier, A., & Escartin, J. (2007). Dynamic control on serpentine crystallization in veins: Constraints on hydration processes in oceanic peridotites. *Geochemistry, Geophysics, Geosystems*, *8*(2), Q02012. https://doi.org/10.1029/2006gc001373

Angiboust, S., Agard, P., Jolivet, L., & Beyssac, O. (2009). The Zermatt-Saas ophiolite: The largest (60-km wide) and deepest (c. 70–80 km) continuous slice of oceanic lithosphere detached from a subduction zone? *Terra Nova*, *21*(3), 171–180. https://doi.org/10.1111/j.1365-3121.2009.00870.x

Auzemery, A., Willingshofer, E., Yamato, P., Duretz, T., & Sokoutis, D. (2020). Strain localization mechanisms for subduction initiation at passive margins. *Global and Planetary Change*, *195*, 103323. https://doi.org/10.1016/j.gloplacha.2020.103323

Babist, J., Handy, M., Konrad-Schmolke, M., & Hammerschmidt, K. (2006). Precollisional, multistage exhumation of subducted continental crust: The Sesia Zone, Western Alps. *Tectonics*, *25*(6), TC6008. https://doi.org/10.1029/2005tc001927

Barnicoat, A., Rex, D., Guise, P., & Cliff, R. (1995). The timing of and nature of greenschist facies deformation and metamorphism in the upper Pennine Alps. *Tectonics*, *14*(2), 279–293. https://doi.org/10.1029/94tc02017

Barrow, G. (1893). On an intrusion of muscovite-biotite gneiss in the South-eastern highlands of Scotland, and its accompanying metamorphism. *Quarterly Journal of the Geological Society*, *49*(1–4), 330–358. https://doi.org/10.1144/gsl.jgs.1893.049.01-04.52

Beaussier, S. J., Gerya, T. V., & Burg, J.-P. (2019). 3D numerical modelling of the Wilson cycle: Structural inheritance of alternating subduction polarity. *Geological Society, London, Special Publications*, *470*(1), 439–461. https://doi.org/10.1144/sp470.15

Beltrando, M., Compagnoni, R., & Lombardo, B. (2010). (Ultra-)high-pressure metamorphism and orogenesis: An alpine perspective. *Gondwana Research*, *18*(1), 147–166. https://doi.org/10.1016/j.gr.2010.01.009

Beltrando, M., Lister, G. S., Rosenbaum, G., Richards, S., & Forster, M. A. (2010). Recognizing episodic lithospheric thinning along a convergent plate margin: The example of the Early Oligocene Alps. *Earth-Science Reviews*, *103*(3–4), 81–98. https://doi.org/10.1016/j.earscirev.2010.09.001

Berger, A., & Bousquet, R. (2008). Subduction-related metamorphism in the Alps: Review of isotopic ages based on petrology and their geodynamic consequences. *Geological Society, London, Special Publications*, *298*(1), 117–144. https://doi.org/10.1144/sp298.7

Berger, A., Schmid, S. M., Engi, M., Bousquet, R., & Wiederkehr, M. (2011). Mechanisms of mass and heat transport during Barrovian metamorphism: A discussion based on field evidence from the Central Alps (Switzerland/Northern Italy). *Tectonics*, *30*(1), 2009TC002622. https://doi.org/10.1029/2009tc002622

Bonnet, G., Chopin, C., Locatelli, M., Kylander-Clark, A. R. C., & Hacker, B. R. (2022). Protracted subduction of the European hyperextended margin revealed by rutile U-Pb geochronology across the Dora-Maira Massif (Western Alps). *Tectonics*, *41*(4), e2021TC007170. https://doi.org/10.1029/2021TC007170

Bousquet, R., Goffé, B., Vidal, O., Oberhänsli, R., & Patriat, M. (2002). The tectono-metamorphic history of the Valaisan domain from the Western to the Central Alps: New constraints on the evolution of the Alps. *The Geological Society of America Bulletin*, *114*(2), 207–225. https://doi.org/10.1130/0016-7606(2002)114<0207:ttmhot>2.0.co;2

Bousquet, R., Oberhänsli, R., Goffé, B., Wiederkehr, M., Koller, F., Schmid, S. M., et al. (2008). Metamorphism of metasediments at the scale of an orogen: A key to the tertiary geodynamic evolution of the Alps. *Geological Society, London, Special Publications*, *298*(1), 393–411. https://doi.org/10.1144/sp298.18

Bucher, S., Schmid, S. M., Bousquet, R., & Fügenschuh, B. (2003). Late-stage deformation in a collisional orogen (Western Alps): Nappe refolding, back-thrusting or normal faulting? *Terra Nova*, *15*(2), 109–117. https://doi.org/10.1046/j.1365-3121.2003.00470.x

Burg, J., & Gerya, T. (2005). The role of viscous heating in Barrovian metamorphism of collisional orogens: Thermomechanical models and application to the Lepontine Dome in the Central Alps. *Journal of Metamorphic Geology*, *23*(2), 75–95. https://doi.org/10.1111/j.1525-1314.2005.00563.x

Burov, E., François, T., Agard, P., Le Pourhiet, L., Meyer, B., Tirel, C., et al. (2014). Rheological and geodynamic controls on the mechanisms of subduction and HP/UHP exhumation of crustal rocks during continental collision: Insights from numerical models. *Tectonophysics*, *631*, 212–250. https://doi.org/10.1016/j.tecto.2014.04.033

Burov, E., Jolivet, L., Le Pourhiet, L., & Poliakov, A. (2001). A thermomechanical model of exhumation of high pressure (HP) and ultra-high pressure (UHP) metamorphic rocks in alpine-type collision belts. *Tectonophysics*, *342*(1–2), 113–136. https://doi.org/10.1016/s0040-1951(01)00158-5

Butler, J. P., Beaumont, C., & Jamieson, R. A. (2014). The Alps 2: Controls on crustal subduction and (ultra)high-pressure rock exhumation in alpine-type orogens. *Journal of Geophysical Research: Solid Earth*, *119*(7), 5987–6022. https://doi.org/10.1002/2013jb010799

Campani, M., Herman, F., & Mancktelow, N. (2010). Two-and three-dimensional thermal modeling of a low-angle detachment: Exhumation history of the Simplon Fault Zone, Central Alps. *Journal of Geophysical Research*, *115*(B10), B10420. https://doi.org/10.1029/2009jb007036

Campani, M., Mancktelow, N., Seward, D., Rolland, Y., Müller, W., & Guerra, I. (2010). Geochronological evidence for continuous exhumation through the ductile-brittle transition along a crustal-scale low-angle normal fault: Simplon Fault Zone, Central Alps. *Tectonics*, *29*(3), 2009TC002582. https://doi.org/10.1029/2009tc002582

Candioti, L. G., Duretz, T., & Schmalholz, S. M. (2022). Horizontal force required for subduction initiation at passive margins with constraints from slab detachment. *Frontiers of Earth Science*, *10*, 785418. https://doi.org/10.3389/feart.2022.785418

Candioti, L. G., Moulas, E., Duretz, T., & Schmalholz, S. M. (2021). Buoyancy versus shear forces in building orogenic wedges. *Solid Earth*, *12*(8), 1749–1775. https://doi.org/10.5194/se-12-1749-2021

Candioti, L. G., Schmalholz, S. M., & Duretz, T. (2020). Impact of upper mantle convection on lithosphere hyperextension and subsequent horizontally forced subduction initiation. *Solid Earth*, *11*(6), 2327–2357. https://doi.org/10.5194/se-11-2327-2020

Cawood, T. K., & Platt, J. P. (2020). Variations in the P-T-t of deformation in a crustal-scale shear zone in metagranite. *Geochemistry, Geophysics, Geosystems*, *21*(11), e2020GC009384. https://doi.org/10.1029/2020GC009384

Challandes, N., Marquer, D., & Villa, I. M. (2003). Dating the evolution of C–S microstructures: A combined $^{40}Ar/^{39}Ar$ step-heating and UV laserprobe analysis of the Alpine Roffna shear zone. *Chemical Geology*, *197*(1–4), 3–19. https://doi.org/10.1016/s0009-2541(02)00354-6

Chang, C.-P., Angelier, J., & Huang, C.-Y. (2009). Evolution of subductions indicated by mélanges in Taiwan. In *Subduction zone geodynamics* (pp. 207–225). Springer.

Chemenda, A. I., Mattauer, M., Malavieille, J., & Bokun, A. N. (1995). A mechanism for syn-collisional rock exhumation and associated normal faulting: Results from physical modelling. *Earth and Planetary Science Letters*, *132*(1–4), 225–232. https://doi.org/10.1016/0012-821x(95)00042-b

Chenin, P., Picazo, S., Jammes, S., Manatschal, G., Müntener, O., & Karner, G. (2019). Potential role of lithospheric mantle composition in the Wilson cycle: A North Atlantic perspective. *Geological Society, London, Special Publications*, *470*(1), 157–172. https://doi.org/10.1144/sp470.10

Chian, D., Louden, K. E., Minshull, T. A., & Whitmarsh, R. B. (1999). Deep structure of the ocean-continent transition in the southern Iberia Abyssal Plain from seismic refraction profiles: Ocean Drilling Program (Legs 149 and 173) transect. *Journal of Geophysical Research*, *104*(B4), 7443–7462. https://doi.org/10.1029/1999jb900004

Chopin, C. (1984). Coesite and pure pyrope in high-grade blueschists of the Western Alps: A first record and some consequences. *Contributions to Mineralogy and Petrology*, *86*(2), 107–118. https://doi.org/10.1007/bf00381838

Chopin, C. (1987). Very-high-pressure metamorphism in the Western Alps: Implications for subduction of continental crust. *Philosophical Transactions of the Royal Society of London – Series A: Mathematical and Physical Sciences*, *321*(1557), 183–197. https://doi.org/10.1098/rsta.1987.0010

Connolly, J., & Petrini, K. (2002). An automated strategy for calculation of phase diagram sections and retrieval of rock properties as a function of physical conditions. *Journal of Metamorphic Geology*, *20*(7), 697–708. https://doi.org/10.1046/j.1525-1314.2002.00398.x

Cortiana, G., Dal Piaz, G., Del Moro, A., Hunziker, J., & Martin, S. (1998). ^{40}Ar-^{39}Ar and Rb-Sr dating of the Pillonet klippe and Sesia-Lanzo basal slice in the Ayas valley and evolution of the Austroalpine-Piedmont nappe stack. *Memorie di Scienze Geologiche*, *50*, 177–194.

Crameri, F. (2018). Geodynamic diagnostics, scientific visualisation and StagLab 3.0. *Geoscientific Model Development*, *11*(6), 2541–2562. https://doi.org/10.5194/gmd-11-2541-2018

Dal Piaz, G., Cortiana, G., Del Moro, A., Martin, S., Pennacchioni, G., & Tartarotti, P. (2001). Tertiary age and paleostructural inferences of the eclogitic imprint in the Austroalpine outliers and Zermatt–Saas ophiolite, Western Alps. *International Journal of Earth Sciences*, *90*(3), 668–684. https://doi.org/10.1007/s005310000177

De Graciansky, P.-C., Roberts, D. G., & Tricart, P. (2011). The birth of the Western and Central Alps: Subduction, obduction, collision. In *Developments in Earth Surface Processes* (Vol. 14, pp. 289–315). Elsevier.

Dewey, J., Helman, M., Knott, S., Turco, E., & Hutton, D. (1989). Kinematics of the western Mediterranean. *Geological Society, London, Special Publications*, *45*(1), 265–283. https://doi.org/10.1144/gsl.sp.1989.045.01.15

Dewey, J. F., & Burke, K. (1974). Hot spots and continental break-up: Implications for collisional orogeny. *Geology*, *2*(2), 57–60. https://doi.org/10.1130/0091-7613(1974)2<57:hsacbi>2.0.co;2

Di Vincenzo, G., Tonarini, S., Lombardo, B., Castelli, D., & Ottolini, L. (2006). Comparison of ^{40}Ar–^{39}Ar and Rb–Sr data on phengites from the UHP Brossasco–Isasca unit (Dora Maira Massif, Italy): Implications for dating white mica. *Journal of Petrology*, *47*(7), 1439–1465. https://doi.org/10.1093/petrology/egl018

Duchêne, S., Blichert-Toft, J., Luais, B., Télouk, P., Lardeaux, J.-M., & Albarede, F. (1997). The Lu–Hf dating of garnets and the ages of the Alpine high-pressure metamorphism. *Nature*, *387*(6633), 586–589. https://doi.org/10.1038/42446

Duretz, T., Gerya, T., Kaus, B., & Andersen, T. (2012). Thermomechanical modeling of slab eduction. *Journal of Geophysical Research*, *117*(B8), B08411. https://doi.org/10.1029/2012jb009137

Duretz, T., Petri, B., Mohn, G., Schmalholz, S., Schenker, F., & Müntener, O. (2016). The importance of structural softening for the evolution and architecture of passive margins. *Scientific Reports*, *6*(1), 1–7. https://doi.org/10.1038/srep38704

Engi, M., Regis, D., Darling, J., Rubatto, D., Cenki Tok, B., Zucali, M., & Compagnoni, R. (2011). *Dynamics in the Sesia HP terrane: Combined petrochronological and structural analysis*. Intervento presentato al convegno Nature of the plate interface in subduction zones tenutosi a Monviso nel 2011.

Engi, M., Todd, C., & Schmatz, D. (1995). Tertiary metamorphic conditions in the eastern Lepontine Alps. *Schweizerische Mineralogische und Petrographische Mitteilungen*, *75*(3), 347–369.

England, P., & Holland, T. (1979). Archimedes and the Tauern eclogites: The role of buoyancy in the preservation of exotic eclogite blocks. *Earth and Planetary Science Letters*, *44*(2), 287–294. https://doi.org/10.1016/0012-821X(79)90177-8

Erdős, Z., Huismans, R. S., & Beek, P. v. d. (2019). Control of increased sedimentation on orogenic fold-and-thrust belt structure–insights into the evolution of the Western Alps. *Solid Earth*, *10*(2), 391–404. https://doi.org/10.5194/se-10-391-2019

Ernst, W. (1971). Metamorphic zonations on presumably subducted lithospheric plates from Japan, California and the Alps. *Contributions to Mineralogy and Petrology*, *34*(1), 43–59. https://doi.org/10.1007/bf00376030

Ernst, W. (1972). Occurrence and mineralogic evolution of blueschist belts with time. *American Journal of Science*, *272*(7), 657–668. https://doi.org/10.2475/ajs.272.7.657

Escher, A., & Beaumont, C. (1997). Formation, burial and exhumation of basement nappes at crustal scale: A geometric model based on the western Swiss-Italian Alps. *Journal of Structural Geology*, *19*(7), 955–974. https://doi.org/10.1016/s0191-8141(97)00022-9

Escher, A., Hunziker, J., Marthaler, M., Masson, H., Sartori, M., & Steck, A. (1997). Geological framework and structural evolution of the western Swiss-Italian Alps. *Deep Structure of the Swiss Alps: Results of the National Research Program*, *20*(NRP 20), 205–222.

Escher, A., Masson, H., & Steck, A. (1993). Nappe geometry in the western Swiss Alps. *Journal of Structural Geology*, *15*(3–5), 501–509. https://doi.org/10.1016/0191-8141(93)90144-y

Eskola, P. (1915). On the relations between the chemical and mineralogical composition in the metamorphic rocks of Orijarvi region. *Bull. Comm. Géol. Finlande*, *44*.

Ferrando, S., Bernoulli, D., & Compagnoni, R. (2004). The Canavese zone (internal Western Alps): A distal margin of Adria. *Schweizerische Mineralogische und Petrographische Mitteilungen*, *84*(1–20), 237–259.

Forster, M., Lister, G., Compagnoni, R., Giles, D., Hills, Q., Betts, P., et al. (2004). Mapping of oceanic crust with "HP" to "UHP" metamorphism: The Lago di Cignana Unit (Western Alps). In *Mapping Geology in Italy*. Geological Society of London.

Frey, M., Desmons, J., & Neubauer, F. (1999). Metamorphic maps of the Alps. An enclosure to. *Schweizerische Mineralogische und Petrographische Mitteilungen*, *79*(1), 1–4.

Froitzheim, N., Pleuger, J., & Nagel, T. J. (2006). Extraction faults. *Journal of Structural Geology*, *28*(8), 1388–1395. https://doi.org/10.1016/j.jsg.2006.05.002

Froitzheim, N., Pleuger, J., Roller, S., & Nagel, T. (2003). Exhumation of high-and ultrahigh-pressure metamorphic rocks by slab extraction. *Geology*, *31*(10), 925–928. https://doi.org/10.1130/g19748.1

Gasinski, A., Slaczka, A., & Winkler, W. (1997). Tectono-sedimentary evolution of the Upper Prealpine Nappe (Switzerland and France): Nappe formation by Late Cretaceous-Paleogene accretion. *Geodinamica Acta*, *10*(4), 137–157. https://doi.org/10.1080/09853111.1997.11105299

Gebauer, D., Schertl, H.-P., Brix, M., & Schreyer, W. (1997). 35 Ma old ultrahigh-pressure metamorphism and evidence for very rapid exhumation in the Dora Maira Massif, Western Alps. *Lithos*, *41*(1–3), 5–24. https://doi.org/10.1016/s0024-4937(97)82002-6

Gerya, T. (2015). Tectonic overpressure and underpressure in lithospheric tectonics and metamorphism. *Journal of Metamorphic Geology*, *33*(8), 785–800. https://doi.org/10.1111/jmg.12144

Gerya, T., Stöckhert, B., & Perchuk, A. L. (2002). Exhumation of high-pressure metamorphic rocks in a subduction channel: A numerical simulation. *Tectonics*, *21*(6), 6-1–6-19. https://doi.org/10.1029/2002tc001406

Gerya, T., & Yuen, D. (2003). Characteristics-based marker-in-cell method with conservative finite-differences schemes for modeling geological flows with strongly variable transport properties. *Physics of the Earth and Planetary Interiors*, *140*(4), 293–318. https://doi.org/10.1016/j.pepi.2003.09.006

Ghent, E. (2020). Metamorphic facies: A review and some suggestions for changes. *The Canadian Mineralogist*, *58*(4), 437–444. https://doi.org/10.3749/canmin.1900078

Gianola, O., Schmidt, M. W., von Quadt, A., Peytcheva, I., Luraschi, P., & Reusser, E. (2014). Continuity in geochemistry and time of the Tertiary Bergell intrusion (Central Alps). *Swiss Journal of Geosciences*, *107*(2), 197–222. https://doi.org/10.1007/s00015-014-0174-8

Goffé, B., & Bousquet, R. (1997). Ferrocarpholite, chloritoid and lawsonite in metapelites of the Versoyen and Petit St Bernard units (Valais zone, Western Alps). *Schweizerische Mineralogische und Petrographische Mitteilungen*, *77*(2), 137–147.

Gregory, C. J., McFarlane, C. R., Hermann, J., & Rubatto, D. (2009). Tracing the evolution of calc-alkaline magmas: In-situ Sm–Nd isotope studies of accessory minerals in the Bergell Igneous Complex, Italy. *Chemical Geology*, *260*(1–2), 73–86. https://doi.org/10.1016/j.chemgeo.2008.12.003

Groppo, C., Ferrando, S., Gilio, M., Botta, S., Nosenzo, F., Balestro, G., et al. (2019). What's in the sandwich? New P–T constraints for the (U)HP nappe stack of southern Dora-Maira Massif (Western Alps). *European Journal of Mineralogy*, *31*(4), 665–683. https://doi.org/10.1127/ejm/2019/0031-2860

Guillot, S., & Hattori, K. (2013). Serpentinites: Essential roles in geodynamics, arc volcanism, sustainable development, and the origin of life. *Elements*, *9*(2), 95–98. https://doi.org/10.2113/gselements.9.2.95

Guillot, S., Schwartz, S., Reynard, B., Agard, P., & Prigent, C. (2015). Tectonic significance of serpentinites. *Tectonophysics*, *646*, 1–19. https://doi.org/10.1016/j.tecto.2015.01.020

Hacker, B. R., & Gerya, T. V. (2013). Paradigms, new and old, for ultrahigh-pressure tectonism. *Tectonophysics*, *603*, 79–88. https://doi.org/10.1016/j.tecto.2013.05.026

Handy, M. R., Ustaszewski, K., & Kissling, E. (2015). Reconstructing the Alps–Carpathians–Dinarides as a key to understanding switches in subduction polarity, slab gaps and surface motion. *International Journal of Earth Sciences*, *104*(1), 1–26. https://doi.org/10.1007/s00531-014-1060-3

Hess, H. (1955). Serpentines, orogeny, and epeirogeny. *Geological Society of America Special Paper*, *62*, 391–407. https://doi.org/10.1130/SPE62-p391

Hilairet, N., Reynard, B., Wang, Y., Daniel, I., Merkel, S., Nishiyama, N., & Petitgirard, S. (2007). High-pressure creep of serpentine, interseismic deformation, and initiation of subduction. *Science*, *318*(5858), 1910–1913. https://doi.org/10.1126/science.1148494

Hirth, G., & Kohlstedt, D. (2003). Rheology of the upper mantle and the mantle wedge: A view from the experimentalists. *Geophysical Monograph-American Geophysical Union*, *138*, 83–106.

Inger, S., Ramsbotham, W., Cliff, R., & Rex, D. (1996). Metamorphic evolution of the Sesia-Lanzo Zone, Western Alps: Time constraints from multi-system geochronology. *Contributions to Mineralogy and Petrology*, *126*(1–2), 152–168. https://doi.org/10.1007/s004100050241

Isacks, B., Oliver, J., & Sykes, L. R. (1968). Seismology and the new global tectonics. *Journal of Geophysical Research*, *73*(18), 5855–5899. https://doi.org/10.1016/0040-1951(69)90024-9

Jamieson, R. A., Beaumont, C., Fullsack, P., & Lee, B. (1998). Barrovian regional metamorphism: Where's the heat? *Geological Society, London, Special Publications*, *138*(1), 23–51. https://doi.org/10.1144/gsl.sp.1996.138.01.03

Jamtveit, B., Moulas, E., Andersen, T. B., Austrheim, H., Corfu, F., Petley-Ragan, A., & Schmalholz, S. M. (2018). High pressure metamorphism caused by fluid induced weakening of deep continental crust. *Scientific Reports*, *8*(1), 1–8. https://doi.org/10.1038/s41598-018-35200-1

Keller, L. M., Hess, M., Fügenschuh, B., & Schmid, S. M. (2005). Structural and metamorphic evolution of the Camughera–Moncucco, Antrona and Monte Rosa units southwest of the Simplon line, Western Alps. *Eclogae Geologicae Helvetiae*, *98*(1), 19–49. https://doi.org/10.1007/s00015-005-1149-6

Kiss, D., Candioti, L. G., Duretz, T., & Schmalholz, S. M. (2020). Thermal softening induced subduction initiation at a passive margin. *Geophysical Journal International*, *220*(3), 2068–2073. https://doi.org/10.1093/gji/ggz572

Kiss, D., Podladchikov, Y., Duretz, T., & Schmalholz, S. M. (2019). Spontaneous generation of ductile shear zones by thermal softening: Localization criterion, 1D to 3D modelling and application to the lithosphere. *Earth and Planetary Science Letters*, *519*, 284–296. https://doi.org/10.1016/j.epsl.2019.05.026

Kurz, W., & Froitzheim, N. (2002). The exhumation of eclogite-facies metamorphic rocks—A review of models confronted with examples from the Alps. *International Geology Review*, *44*(8), 702–743. https://doi.org/10.2747/0020-6814.44.12.1163

Lardeaux, J.-M. (2014). Deciphering orogeny: A metamorphic perspective. Examples from European Alpine and Variscan belts: Part I: Alpine metamorphism in the Western Alps. A review. *Bulletin de la Societe Geologique de France*, *185*(2), 93–114. https://doi.org/10.2113/gssgfbull.185.2.93

Lardeaux, J.-M., Gosso, G., Kienast, J. R., & Lombardo, B. (1982). Relations entre le metamorphisme et la deformation dans la zone Sesia-Lanzo (Alpes Occidentales) et le probleme de l'eclogitisation de la croute continentale. *Bulletin de la Société Géologique de France*, *S7-XXIV*(4), 793–800. https://doi.org/10.2113/gssgfbull.S7-XXIV.4.793

Le Breton, E., Brune, S., Ustaszewski, K., Zahirovic, S., Seton, M., & Müller, R. D. (2021). Kinematics and extent of the Piemont–Liguria Basin–implications for subduction processes in the Alps. *Solid Earth*, *12*(4), 885–913. https://doi.org/10.5194/se-12-885-2021

Lemoine, M., Bas, T., Arnaud-Vanneau, A., Arnaud, H., Dumont, T., Gidon, M., et al. (1986). The continental margin of the Mesozoic Tethys in the Western Alps. *Marine and Petroleum Geology*, *3*(3), 179–199. https://doi.org/10.1016/0264-8172(86)90044-9

Le Pichon, X. (1968). Sea-floor spreading and continental drift. *Journal of Geophysical Research*, *73*(12), 3661–3697. https://doi.org/10.1029/jb073i012p03661

Liao, J., Malusà, M. G., Zhao, L., Baldwin, S. L., Fitzgerald, P. G., & Gerya, T. (2018). Divergent plate motion drives rapid exhumation of (ultra) high pressure rocks. *Earth and Planetary Science Letters*, *491*, 67–80. https://doi.org/10.1016/j.epsl.2018.03.024

Luisier, C., Baumgartner, L., Schmalholz, S. M., Siron, G., & Vennemann, T. (2019). Metamorphic pressure variation in a coherent Alpine nappe challenges lithostatic pressure paradigm. *Nature Communications*, *10*(1), 1–11. https://doi.org/10.1038/s41467-019-12727-z

Luisier, C., Baumgartner, L. P., Putlitz, B., & Vennemann, T. (2021). Whiteschist Genesis through metasomatism and metamorphism in the Monte Rosa nappe (Western Alps). *Contributions to Mineralogy and Petrology*, *176*(1), 1–24. https://doi.org/10.1007/s00410-020-01759-0

Malusà, M. G., Faccenna, C., Baldwin, S. L., Fitzgerald, P. G., Rossetti, F., Balestrieri, M. L., et al. (2015). Contrasting styles of (U) HP rock exhumation along the Cenozoic Adria-Europe plate boundary (Western Alps, Calabria, Corsica). *Geochemistry, Geophysics, Geosystems*, *16*(6), 1786–1824. https://doi.org/10.1002/2015gc005767

Malusà, M. G., Guillot, S., Zhao, L., Paul, A., Solarino, S., Dumont, T., et al. (2021). The deep structure of the Alps based on the CIFALPS seismic experiment: A synthesis. *Geochemistry, Geophysics, Geosystems*, *22*(3), e2020GC009466. https://doi.org/10.1029/2020gc009466

Mancktelow, N. (1985). The Simplon Line: A major displacement zone in the western Lepontine Alps. *Eclogae Geologicae Helvetiae*, *78*(1), 73–96.

Mancktelow, N. S. (2008). Tectonic pressure: Theoretical concepts and modelled examples. *Lithos*, *103*(1–2), 149–177. https://doi.org/10.1016/j.lithos.2007.09.013

Manzotti, P., Ballevre, M., Zucali, M., Robyr, M., & Engi, M. (2014). The tectonometamorphic evolution of the Sesia–Dent Blanche nappes (internal Western Alps): Review and synthesis. *Swiss Journal of Geosciences*, *107*(2), 309–336. https://doi.org/10.1007/s00015-014-0172-x

Manzotti, P., Bosse, V., Pitra, P., Robyr, M., Schiavi, F., & Ballevre, M. (2018). Exhumation rates in the Gran Paradiso Massif (Western Alps) constrained by in situ U–Th–Pb dating of accessory phases (monazite, allanite and xenotime). *Contributions to Mineralogy and Petrology*, *173*(3), 24. https://doi.org/10.1007/s00410-018-1452-7

Manzotti, P., Zucali, M., Ballevre, M., Robyr, M., & Engi, M. (2014). Geometry and kinematics of the Roisan-Cignana Shear Zone, and the orogenic evolution of the Dent Blanche Tectonic System (Western Alps). *Swiss Journal of Geosciences*, *107*(1), 23–47. https://doi.org/10.1007/s00015-014-0157-9

McCarthy, A., Tugend, J., Mohn, G., Candioti, L., Chelle-Michou, C., Arculus, R., et al. (2020). A case of Ampferer-type subduction and consequences for the Alps and the Pyrenees. *American Journal of Science*, *320*(4), 313–372. https://doi.org/10.2475/04.2020.01

Miyashiro, A. (2012). *Metamorphism and metamorphic belts*. Springer Science & Business Media.

Mohn, G., Manatschal, G., Müntener, O., Beltrando, M., & Masini, E. (2010). Unravelling the interaction between tectonic and sedimentary processes during lithospheric thinning in the Alpine Tethys margins. *International Journal of Earth Sciences*, *99*(1), 75–101. https://doi.org/10.1007/s00531-010-0566-6

Morgan, W. J. (1968). Rises, trenches, great faults, and crustal blocks. *Journal of Geophysical Research*, *73*(6), 1959–1982. https://doi.org/10.1029/jb073i006p01959

Moulas, E., Podladchikov, Y. Y., Aranovich, L. Y., & Kostopoulos, D. (2013). The problem of depth in geology: When pressure does not translate into depth. *Petrology*, *21*(6), 527–538. https://doi.org/10.1134/s0869591113060052

Nibourel, L., Berger, A., Egli, D., Heuberger, S., & Herwegh, M. (2021). Structural and thermal evolution of the eastern Aar Massif: Insights from structural field work and Raman thermometry. *Swiss Journal of Geosciences*, *114*(1), 1–43. https://doi.org/10.1186/s00015-020-00381-3

Oberhänsli, R., Bousquet, R., Engi, M., Goffé, B., Gosso, G., Handy, M., et al. (2004). *Metamorphic structure of the Alps*. CCGM (Commission of the Geological Maps of the World).

Oberli, F., Meier, M., Berger, A., Rosenberg, C. L., & GierÉ, R. (2004). U-Th-Pb and $^{230}Th/^{238}U$ disequilibrium isotope systematics: Precise accessory mineral chronology and melt evolution tracing in the Alpine Bergell intrusion. *Geochimica et Cosmochimica Acta*, *68*(11), 2543–2560. https://doi.org/10.1016/j.gca.2003.10.017

Penniston-Dorland, S. C., Kohn, M. J., & Manning, C. E. (2015). The global range of subduction zone thermal structures from exhumed blueschists and eclogites: Rocks are hotter than models. *Earth and Planetary Science Letters*, *428*, 243–254. https://doi.org/10.1016/j.epsl.2015.07.031

Petri, B., Duretz, T., Mohn, G., Schmalholz, S. M., Karner, G. D., & Müntener, O. (2019). Thinning mechanisms of heterogeneous continental lithosphere. *Earth and Planetary Science Letters*, *512*, 147–162. https://doi.org/10.1016/j.epsl.2019.02.007

Petrini, K., & Podladchikov, Y. (2000). Lithospheric pressure-depth relationship in compressive regions of thickened crust. *Journal of Metamorphic Geology*, *18*(1), 67–77. https://doi.org/10.1046/j.1525-1314.2000.00240.x

Philpotts, A., & Ague, J. (2009). *Principles of igneous and metamorphic petrology*. Cambridge University Press.

Putnis, A., Moore, J., Prent, A. M., Beinlich, A., & Austrheim, H. (2021). Preservation of granulite in a partially eclogitized terrane: Metastable phenomena or local pressure variations? *Lithos*, *400*, 106413. https://doi.org/10.1016/j.lithos.2021.106413

Reddy, S., Wheeler, J., & Cliff, R. (1999). The geometry and timing of orogenic extension: An example from the western Italian Alps. *Journal of Metamorphic Geology*, *17*(5), 573–590. https://doi.org/10.1046/j.1525-1314.1999.00220.x

Reddy, S. M., Wheeler, J., Butler, R. W. H., Cliff, R. A., Freeman, S., Inger, S., et al. (2003). Kinematic reworking and exhumation within the convergent Alpine Orogen. *Tectonophysics*, *365*(1–4), 77–102. https://doi.org/10.1016/s0040-1951(03)00017-9

Regorda, A., Spalla, M. I., Roda, M., Lardeaux, J., & Marotta, A. M. (2021). Metamorphic facies and deformation fabrics diagnostic of subduction: Insights from 2D numerical models. *Geochemistry, Geophysics, Geosystems*, *22*(10), e2021GC009899. https://doi.org/10.1029/2021gc009899

Ring, U., & Merle, O. (1992). Forethrusting, backfolding, and lateral gravitational escape in the northern part of the Western Alps (Monte Rosa region). *The Geological Society of America Bulletin*, *104*(7), 901–914. https://doi.org/10.1130/0016-7606(1992)104<0901:fbalge>2.3.co;2

Rubatto, D., Gebauer, D., & Compagnoni, R. (1999). Dating of eclogite-facies zircons: The age of Alpine metamorphism in the Sesia–Lanzo Zone (Western Alps). *Earth and Planetary Science Letters*, *167*(3–4), 141–158. https://doi.org/10.1016/s0012-821x(99)00031-x

Rubatto, D., & Hermann, J. (2001). Exhumation as fast as subduction? *Geology*, *29*(1), 3–6. https://doi.org/10.1130/0091-7613(2001)029<0003:eafas>2.0.co;2

Rubatto, D., Hermann, J., Berger, A., & Engi, M. (2009). Protracted fluid-induced melting during Barrovian metamorphism in the Central Alps. *Contributions to Mineralogy and Petrology*, *158*(6), 703–722. https://doi.org/10.1007/s00410-009-0406-5

Ruh, J. B., Le Pourhiet, L., Agard, P., Burov, E., & Gerya, T. (2015). Tectonic slicing of subducting oceanic crust along plate interfaces: Numerical modeling. *Geochemistry, Geophysics, Geosystems*, *16*(10), 3505–3531. https://doi.org/10.1002/2015gc005998

Ryan, P. D., & Dewey, J. F. (2019). The sources of metamorphic heat during collisional orogeny: The Barrovian enigma. *Canadian Journal of Earth Sciences*, *56*(12), 1309–1317. https://doi.org/10.1139/cjes-2018-0182

Saliot, P., Dal Piaz, G., & Frey, M. (1980). Métamorphisme de haute pression dans les Alpes franco-italo-suisses. *Geologie Alpine*, *56*, 203–235.

Schenker, F. L., Schmalholz, S. M., Moulas, E., Pleuger, J., Baumgartner, L. P., Podladchikov, Y., et al. (2015). Current challenges for explaining (ultra)high-pressure tectonism in the Pennine domain of the Central and Western Alps. *Journal of Metamorphic Geology*, *33*(8), 869–886. https://doi.org/10.1111/jmg.12143

Schlunegger, F., & Willett, S. (1999). Spatial and temporal variations in exhumation of the central Swiss Alps and implications for exhumation mechanisms. *Geological Society, London, Special Publications*, *154*(1), 157–179. https://doi.org/10.1144/gsl.sp.1999.154.01.07

Schmalholz, S. M., Duretz, T., Hetényi, G., & Medvedev, S. (2019). Distribution and magnitude of stress due to lateral variation of gravitational potential energy between Indian lowland and Tibetan plateau. *Geophysical Journal International*, *216*(2), 1313–1333. https://doi.org/10.1093/gji/ggy463

Schmalholz, S. M., Medvedev, S., Lechmann, S. M., & Podladchikov, Y. (2014). Relationship between tectonic overpressure, deviatoric stress, driving force, isostasy and gravitational potential energy. *Geophysical Journal International*, *197*(2), 680–696. https://doi.org/10.1093/gji/ggu040

Schmalholz, S. M., Moulas, E., Plümper, O., Myasnikov, A. V., & Podladchikov, Y. Y. (2020). 2D hydro-mechanical-chemical modeling of (de) hydration reactions in deforming heterogeneous rock: The periclase-brucite model reaction. *Geochemistry, Geophysics, Geosystems*, *21*(11), e2020GC009351. https://doi.org/10.1029/2020gc009351

Schmalholz, S. M., & Podladchikov, Y. Y. (2013). Tectonic overpressure in weak crustal-scale shear zones and implications for the exhumation of high-pressure rocks. *Geophysical Research Letters*, *40*(10), 1984–1988. https://doi.org/10.1002/grl.50417

Schmalholz, S. M., & Schenker, F. L. (2016). Exhumation of the Dora Maira ultrahigh-pressure unit by buoyant uprise within a low-viscosity mantle oblique-slip shear zone. *Terra Nova*, *28*(5), 348–355. https://doi.org/10.1111/ter.12227

Schmid, S., & Kissling, E. (2000). The arc of the Western Alps in the light of geophysical data on deep crustal structure. *Tectonics*, *19*(1), 62–85. https://doi.org/10.1029/1999tc900057

Schmid, S. M., Fügenschuh, B., Kissling, E., & Schuster, R. (2004). Tectonic map and overall architecture of the Alpine orogen. *Eclogae Geologicae Helvetiae*, *97*(1), 93–117. https://doi.org/10.1007/s00015-004-1113-x

Schmid, S. M., Kissling, E., Diehl, T., van Hinsbergen, D. J., & Molli, G. (2017). Ivrea mantle wedge, arc of the Western Alps, and kinematic evolution of the Alps–Apennines orogenic system. *Swiss Journal of Geosciences*, *110*(2), 581–612. https://doi.org/10.1007/s00015-016-0237-0

Schmid, S. M., Pfiffner, O.-A., Froitzheim, N., Schönborn, G., & Kissling, E. (1996). Geophysical-geological transect and tectonic evolution of the Swiss-Italian Alps. *Tectonics*, *15*(5), 1036–1064. https://doi.org/10.1029/96tc00433

Schwartz, S., Allemand, P., & Guillot, S. (2001). Numerical model of the effect of serpentinites on the exhumation of eclogitic rocks: Insights from the Monviso ophiolitic massif (Western Alps). *Tectonophysics*, *342*(1–2), 193–206. https://doi.org/10.1016/s0040-1951(01)00162-7

Spear, F. S. (1989). Petrologic determination of metamorphic pressure-temperature-time paths. *Metamorphic Pressure-Temperature-Time Paths*, *7*, 1–55.

Spear, F. S., Pattison, D. R., & Cheney, J. T. (2017). The metamorphosis of metamorphic petrology. The web of geological sciences: Advances, impacts, and interactions II. *Geological Society of America Bulletin*, *523*, 31–73.

Steck, A., & Hunziker, J. (1994). The tertiary structural and thermal evolution of the Central Alps—Compressional and extensional structures in an orogenic belt. *Tectonophysics*, *238*(1–4), 229–254. https://doi.org/10.1016/0040-1951(94)90058-2

Steck, A., Masson, H., & Robyr, M. (2015). Tectonics of the Monte Rosa and surrounding nappes (Switzerland and Italy): Tertiary phases of subduction, thrusting and folding in the Pennine Alps. *Swiss Journal of Geosciences*, *108*(1), 3–34. https://doi.org/10.1007/s00015-015-0188-x

Stöckhert, B., & Gerya, T. V. (2005). Pre-collisional high pressure metamorphism and nappe tectonics at active continental margins: A numerical simulation. *Terra Nova*, *17*(2), 102–110. https://doi.org/10.1111/j.1365-3121.2004.00589.x

Stüwe, K. (1998). Heat sources of cretaceous metamorphism in the Eastern Alps—A discussion. *Tectonophysics*, *287*(1–4), 251–269. https://doi.org/10.1016/s0040-1951(98)80072-3

Tilton, G., Schreyer, W., & Schertl, H.-P. (1989). Pb-Sr-Nd isotopic behavior of deeply subducted crustal rocks from the Dora Maira Massif, Western Alps, Italy. *Geochimica et Cosmochimica Acta*, *53*(6), 1391–1400. https://doi.org/10.1016/0016-7037(89)90071-9

Trümpy, R. (1975). Penninic-Austroalpine boundary in the Swiss Alps: A presumed former continental margin and its problems. *American Journal of Science*, *275*(A), 209–238.

Turcotte, D. L., & Schubert, G. (2002). *Geodynamics*. Cambridge University Press.

Vaughan-Hammon, J. D., Luisier, C., Baumgartner, L. P., & Schmalholz, S. M. (2021a). Alpine peak pressure and tectono-metamorphic history of the Monte Rosa nappe: Evidence from the cirque du Véraz, upper Ayas Valley, Italy. *Swiss Journal of Geosciences*, *114*(1), 1–26. https://doi.org/10.1186/s00015-021-00397-3

Vaughan-Hammon, J. D., Luisier, C., Baumgartner, L. P., & Schmalholz, S. M. (2021b). Peak Alpine metamorphic conditions from staurolite bearing metapelites in the Monte Rosa nappe (central European Alps) and geodynamic implications. *Journal of Metamorphic Geology*, *39*(7), 897–917. https://doi.org/10.1111/jmg.12595

von Blackenburg, F. (1992). Combined high-precision chronometry and geochemical tracing using accessory minerals: Applied to the Central-Alpine Bergell intrusion (central Europe). *Chemical Geology*, *100*(1–2), 19–40. https://doi.org/10.1016/0009-2541(92)90100-j

Vuichard, J., & Ballevre, M. (1988). Garnet–chloritoid equilibria in eclogitic pelitic rocks from the Sesia zone (Western Alps): Their bearing on phase relations in high pressure metapelites. *Journal of Metamorphic Geology*, *6*(2), 135–157. https://doi.org/10.1111/j.1525-1314.1988.tb00413.x

Warren, C. (2013). Exhumation of (ultra-)high-pressure terranes: Concepts and mechanisms. *Solid Earth*, *4*(1), 75–92. https://doi.org/10.5194/se-4-75-2013

Warren, C., Beaumont, C., & Jamieson, R. A. (2008). Modelling tectonic styles and ultra-high pressure (UHP) rock exhumation during the transition from oceanic subduction to continental collision. *Earth and Planetary Science Letters*, *267*(1–2), 129–145. https://doi.org/10.1016/j.epsl.2007.11.025

Wegener, A. (1915). Die entstehung der kontinente und ozeane Braunschweig. *Sammlung Vieweg*, *23*, 94.

Wheeler, J., Reddy, S., & Cliff, R. (2001). Kinematic linkage between internal zone extension and shortening in more external units in the NW Alps. *Journal of the Geological Society*, *158*(3), 439–443. https://doi.org/10.1144/jgs.158.3.439

Wiederkehr, M., Bousquet, R., Schmid, S. M., & Berger, A. (2008). From subduction to collision: Thermal overprint of HP/LT meta-sediments in the north-eastern Lepontine Dome (Swiss Alps) and consequences regarding the tectono-metamorphic evolution of the Alpine orogenic wedge. *Swiss Journal of Geosciences*, *101*(1), 127–155. https://doi.org/10.1007/s00015-008-1289-6

Wiederkehr, M., Bousquet, R., Ziemann, M., Schmid, S., & Berger, A. (2007). *Thermal structure of the Valaisan and Ultra-Helvetic sedimentary units of the northern Lepontine dome—consequences regarding the tectono-metamorphic evolution*. EGU.

Wilson, J. T. (1966). *Did the Atlantic close and then re-open?* 676–681.

Yamato, P., Agard, P., Burov, E., Le Pourhiet, L., Jolivet, L., & Tiberi, C. (2007). Burial and exhumation in a subduction wedge: Mutual constraints from thermomechanical modeling and natural P-T-t data (Schistes Lustrés, Western Alps). *Journal of Geophysical Research*, *112*(B7), B07410. https://doi.org/10.1029/2006jb004441

Yamato, P., Burov, E., Agard, P., Le Pourhiet, L., & Jolivet, L. (2008). HP-UHP exhumation during slow continental subduction: Self-consistent thermodynamically and thermomechanically coupled model with application to the Western Alps. *Earth and Planetary Science Letters*, *271*(1–4), 63–74. https://doi.org/10.1016/j.epsl.2008.03.049

Yang, J., Lu, G., Liu, T., Li, Y., Wang, K., Wang, X., et al. (2020). Amagmatic subduction produced by mantle serpentinization and oceanic crust delamination. *Geophysical Research Letters*, *47*(9), e2019GL086257. https://doi.org/10.1029/2019gl086257